

## RESEARCH ARTICLE

10.1002/2015JB012344

## Key Points:

- First joint CSEM and seismic analysis of an active pockmark at Vestnesa ridge
- Synthetic resistivity models suggested sensitivity to underlying chimney
- Estimated a gas- and hydrate-saturated chimney beneath pockmark supports venting

## Correspondence to:

B. K. Goswami,  
Bedanta.Goswami@noc.soton.ac.uk

## Citation:

Goswami, B. K., K. A. Weitemeyer, T. A. Minshull, M. C. Sinha, G. K. Westbrook, A. Chabert, T. J. Henstock, and S. Ker (2015), A joint electromagnetic and seismic study of an active pockmark within the hydrate stability field at the Vestnesa Ridge, West Svalbard margin, *J. Geophys. Res. Solid Earth*, 120, 6797–6822, doi:10.1002/2015JB012344.

Received 10 JUL 2015

Accepted 7 OCT 2015

Accepted article online 10 OCT 2015

Published online 31 OCT 2015

## A joint electromagnetic and seismic study of an active pockmark within the hydrate stability field at the Vestnesa Ridge, West Svalbard margin

Bedanta K. Goswami<sup>1</sup>, Karen A. Weitemeyer<sup>1</sup>, Timothy A. Minshull<sup>1</sup>, Martin C. Sinha<sup>1</sup>, Graham K. Westbrook<sup>1,2,3</sup>, Anne Chabert<sup>1,4</sup>, Timothy J. Henstock<sup>1</sup>, and Stephan Ker<sup>3</sup>

<sup>1</sup>Ocean and Earth Science, University of Southampton, National Oceanography Centre Southampton, Southampton, UK,

<sup>2</sup>School of Geography, Earth and Environmental Sciences, University of Birmingham, Birmingham, UK, <sup>3</sup>Geosciences Marines, Ifremer Centre de Brest, Plouzané, France, <sup>4</sup>Fugro EMU Ltd., Southampton, UK

**Abstract** We acquired coincident marine controlled source electromagnetic (CSEM), high-resolution seismic reflection and ocean-bottom seismometer (OBS) data over an active pockmark in the crest of the southern part of the Vestnesa Ridge, to estimate fluid composition within an underlying fluid-migration chimney. Synthetic model studies suggest resistivity obtained from CSEM data can resolve gas or hydrate saturation greater than 5% within the chimney. Acoustic chimneys imaged by seismic reflection data beneath the pockmark and on the ridge flanks were found to be associated with high-resistivity anomalies (+2–4  $\Omega$ m). High-velocity anomalies (+0.3 km/s), within the gas-hydrate stability zone (GHSZ) and low-velocity anomalies (–0.2 km/s) underlying the GHSZ, were also observed. Joint analysis of the resistivity and velocity anomaly indicates pore saturation of up to 52% hydrate with 28% free gas, or up to 73% hydrate with 4% free gas, within the chimney beneath the pockmark assuming a nonuniform and uniform fluid distribution, respectively. Similarly, we estimate up to 30% hydrate with 4% free gas or 30% hydrate with 2% free gas within the pore space of the GHSZ outside the central chimney assuming a nonuniform and uniform fluid distribution, respectively. High levels of free-gas saturation in the top part of the chimney are consistent with episodic gas venting from the pockmark.

### 1. Introduction

Gas hydrates are naturally occurring solid substances containing a gas molecule within a rigid cage of water molecules that form at low temperatures and high pressures [Kvenvolden, 1999]. In 80% of naturally occurring gas hydrates, the constituent gas is methane, although carbon dioxide, hydrogen sulphide, ethane, propane, and isobutane can also form hydrates [Kvenvolden, 1993; Sloan et al., 1998]. Hydrate formation is mainly controlled by temperature, pressure, gas concentration, pore fluid salinity, and the nature of the gas enclosed [Sloan and Koh, 2008]. The Vestnesa Ridge, located on the West Svalbard continental margin, is an area where gas hydrates are stable within the top 200 m of sediments below the seafloor [Vogt et al., 1994; Hustoft et al., 2009; Bünz et al., 2012; Smith et al., 2014a]. The presence of gas hydrate in the area was predicted from the observation of a discontinuous bottom simulating reflector (BSR) in seismic reflection data [Vogt et al., 1994]. High seismic velocities near the interpreted base of gas hydrate stability zone (GHSZ) [Hustoft et al., 2009], further supported the argument for hydrate presence, which was later confirmed by the recovery of hydrates in a shallow sediment core collected from the pockmark in 2008 [Fisher et al., 2011].

The discovery of numerous pockmarks with episodic methane venting along the crest of the Vestnesa Ridge [Hustoft et al., 2009; Fisher et al., 2011; Bünz et al., 2012; Smith et al., 2014a] has caused increased scientific interest over the last decade to understand the dynamics of the gas/gas hydrate system beneath these pockmarks. Acoustic flares observed on hydroacoustic data show that some bubbles occasionally reach the upper mixed layer of the ocean ( $\leq 400$  m in NW of Svalbard) [de Boye Montegut et al., 2004; Hustoft et al., 2009; Bünz et al., 2012; Smith et al., 2014a]. Geochemical analysis of gas and hydrate sampled at the Vestnesa pockmarks contain a strong thermogenic signature [Fisher et al., 2011; Smith et al., 2014a; Panieri et al., 2014], which suggest the venting gas migrates from depth and escapes through the GHSZ. The origin of the thermogenic gas is

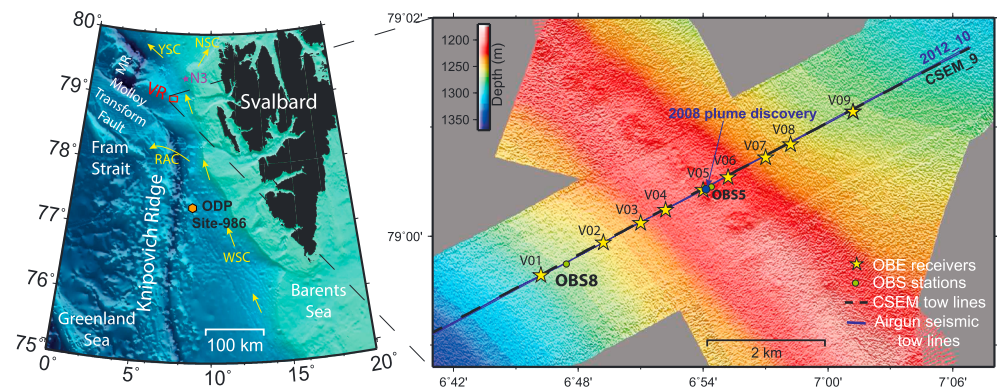


**Figure 1.** Map of west Svalbard highlighting the Vestnesa Ridge survey area on the regional bathymetry map from international bathymetric chart of the Arctic Ocean (IBCAO) data [Jakobsson *et al.*, 2008]. The zoomed survey area map shows the location of the coincident CSEM and seismic survey overlaid on top of multibeam bathymetry data acquired in 2011. CSEM-Line9 and 2012-10 are used along with velocity profile obtained from the OBS sites to interpret subsurface properties across the ridge over an active pockmark discovered in 2008 [Westbrook *et al.*, 2009]. VR = Vestnesa, MR = Molloy Ridge, N3 = OBS Site [Chabert *et al.*, 2011], WSC = West Spitsbergen Current, RAC = Return Atlantic Current, NSC = North Spitsbergen Current, and YSC = Yermak Slope Current [Sarkar *et al.*, 2012; Gebhardt *et al.*, 2014].

inferred to be early Miocene source rocks [Smith *et al.*, 2014a]. Acoustic chimneys imaged by seismic reflection data underneath some of these pockmarks appear to act as migration pathways for the free gas [Hustoft *et al.*, 2009; Bünz *et al.*, 2012; Smith *et al.*, 2014a].

Similar fluid escape features have been observed in other gas hydrate provinces [Bünz, 2004; Tréhu *et al.*, 2004; Torres *et al.*, 2004; Gay *et al.*, 2006; Sultan *et al.*, 2014] which has led to modeling studies, to understand why free gas and gas hydrate coexist within the GHSZ [Liu and Flemings, 2006, 2007; Smith *et al.*, 2014b]. These model studies also address how fluid escape features form and evolve over time to allow free gas to escape. On the basis of seismic reflection data, it has been argued that the chimneys underneath the pockmarks at the Vestnesa Ridge are fed by an overpressured free-gas zone directly below the GHSZ [Hustoft *et al.*, 2009]. Zones of connected free gas with significant depth extent lead to excess pore pressure below the ridge, which subsequently drives free gas toward the seafloor through weaknesses along sediments below the ridge [Vogt *et al.*, 1994; Hustoft *et al.*, 2009].

Marine controlled source electromagnetic (CSEM) data provide a measure of the bulk resistivity of sediments, which is sensitive to the fluid composition in the pore spaces. Gas hydrate and free gas cause an increase in bulk resistivity, while saline pore waters are conductive (low resistivity). Use of CSEM data for marine gas hydrate detection was first suggested by Edwards [1997] and has since been used in various gas hydrate settings around the world [Schwalenberg *et al.*, 2005; Weitemeyer *et al.*, 2006b; Ellis *et al.*, 2008; Schwalenberg *et al.*, 2010; Weitemeyer *et al.*, 2011; Weitemeyer and Constable, 2010]. In this paper, our objective is to estimate the fluid saturations within the fluid-escape features linked to the seafloor pockmarks with the help of coincident CSEM, seismic reflection, and velocity data. This approach will help in evaluating the factors assisting methane gas to escape through the GHSZ.

## 2. Regional Setting

The Vestnesa Ridge is a sediment drift situated on a hot ( $>115 \text{ mW/m}^2$ ) [Hustoft *et al.*, 2009] and young oceanic crust ( $<20 \text{ Ma}$ ) on the eastern flank of the Molloy Ridge in the Fram Strait, west of Svalbard [Vogt *et al.*, 1994; Engen *et al.*, 2008; Petersen *et al.*, 2010] (Figure 1). As part of the West Svalbard continental margin, its stratigraphy has been largely influenced by seafloor spreading, bottom water currents, and glaciation [Eiken and Hinz, 1993; Forsberg *et al.*, 1999]. The boomerang-shaped ridge with the western segment striking  $100^\circ$ , parallel to the Molloy transform and the eastern segment striking  $125^\circ$  contains 2–5 km of late Miocene and Pliocene sediments [Eiken and Hinz, 1993; Howe *et al.*, 2008] deposited by the northward flowing contour currents. Plio-Pleistocene contourite deposits containing glacial debris drape the older contourites, and the very top of the ridge is then covered by silty turbidites and muddy-silty contourites of mid-Weichselian and Holocene age [Howe *et al.*, 2008].

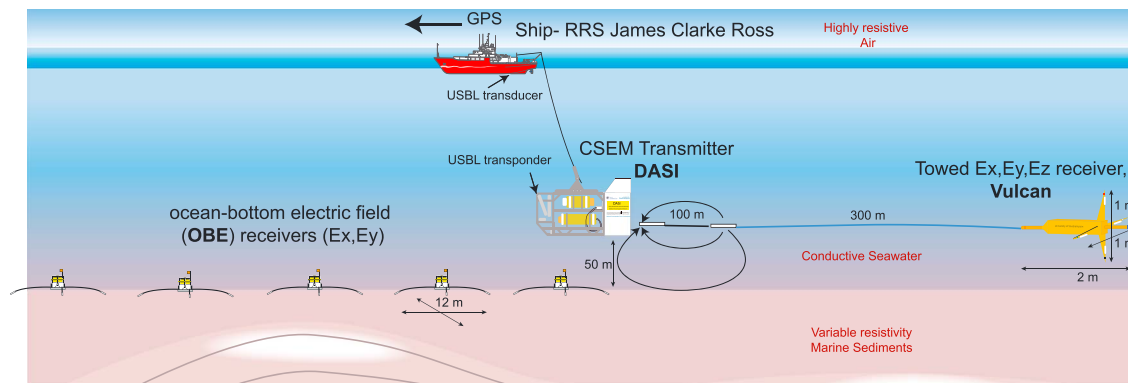


**Figure 2.** Sketch of the CSEM instrument layout used in the 2012 survey at the Vestnesa Ridge. CSEM transmitter, DASI was towed 50 m above the seafloor and transmitted a 81 A current across its 100 m dipole. The towed receiver, Vulcan was attached 300 m behind the DASI antenna and recorded the transmitted EM signal along with the seafloor EM receivers, OBEs (modified from *Weitemeyer and Constable* [2010]).

### 3. Joint Seismic and CSEM Experiment

#### 3.1. Rationale

Current knowledge of gas and hydrate distribution at the Vestnesa Ridge is primarily based on seismic reflection data. An intermittent BSR at the expected base of the GHSZ has been long used as an indicator for gas hydrates at the Vestnesa Ridge [Vogt *et al.*, 1994; Hustoft *et al.*, 2009]. However, free gas is the primary cause of the BSR [Mackay *et al.*, 1994], and hydrate has been discovered in areas with no reported BSR [Paull and Matsumoto, 2000; Haacke *et al.*, 2007]. Seismic velocity anomalies, also used for estimating hydrate and gas saturation, can be obscured by the presence of small amounts of free gas.

Hydrate saturation in pores is often estimated using resistivity measurements during drilling. High resistivity within sediment may be an indicator for hydrate [Collett and Ladd, 2000; Collett *et al.*, 2012] and also free gas-occupying sediment pores [Pearson *et al.*, 1983]. However, other geologic factors such as carbonates, decreased porosity, or pore fluid freshening among others may also lead to high resistivities. While a small concentration of free gas leads to a significant lowering of  $P$  wave velocity, a much larger amount of free gas is required to give the same proportionate rise in resistivity [Constable, 2010]. Colocated seismic and CSEM data were acquired at the Vestnesa Ridge during summer 2011 and 2012 (Figure 1), to identify and measure gas hydrate and free gas saturation using CSEM-derived resistivities and velocity from seismic data.

#### 3.2. CSEM Data Acquisition

We used a deep-towed CSEM transmitter: deep-towed active source instrument (DASI) [Sinha *et al.*, 1990], nine ocean-bottom electric field (OBE) sensors [Minshull *et al.*, 2005], and a deep-towed triaxis electric field receiver—Vulcan [Weitemeyer and Constable, 2010] (Figure 2). DASI was towed 50 m above the seafloor and transmitted a 1 Hz square wave of 81 A current across its 100 m horizontal dipole antenna. A low dipole moment (10 kA m for the fundamental 1 Hz frequency) was chosen to reduce the effect of saturating the electric field preamplifiers. The two orthogonal 12 m long dipoles on each OBE recorded the horizontal components of the electric field at a sampling frequency of 125 Hz. Vulcan was towed 300 m behind the DASI antenna to record the  $E_{\text{vertical}}$  and  $E_{\text{cross line}}$  across its 1 m dipole antennae and  $E_{\text{inline}}$  across its 2 m dipole antenna at 250 Hz sampling frequency.

An ultrashort baseline (USBL) acoustic navigation system was used during the CSEM operation to obtain high accuracy in transmitter positioning. A remotely operated vehicle (ROV), HyBIS [Murton *et al.*, 2012] equipped with a USBL transponder, was used for OBE deployment to obtain accurate placement on the seafloor. OBEs were released from approximately 2–3 m above the planned deployment locations. ROV cameras provided additional confirmation of the OBEs on the seafloor.

#### 3.3. Seismic Data Acquisition

High-resolution seismic data were acquired using a GI gun source (45 cubic inches/2000 psi) that generated useful frequencies up to 300 Hz and a 60-channel streamer with 1 m group spacing. Two ocean bottom seismometers (OBSs) [Minshull *et al.*, 2005] were deployed to record the GI gun source along a profile coincident with the CSEM profile. These instruments were deployed on the seabed using the approach described above for the OBEs and recorded a hydrophone channel and three orthogonal geophone channels, each at 4 kHz

**Table 1.** OBE Dipole Orientations From Geographic North Measured Clockwise Obtained Using OPRA Rotation Code of Key and Lockwood [2010]<sup>a</sup>

Inline Orientation—64.5°		
OBE Site	Orientation Ch-1 ( $E_x$ )	Orientation Ch-2 ( $E_y$ )
V01	105.5°	195.5°
V02	−16.0°	76.0°
V03	101.5°	191.5°
V04	0.5°	90.5°
V05	−50.5°	40.5°
V06	−160.0°	−70.0°
V07	−90.0°	0.0°
V08	−36.0°	66.0°
V10	40.5°	130.5°

<sup>a</sup>The angles obtained have an uncertainty of  $\pm 3^\circ$ .

sample rate. One was deployed on the southwest flank of Vestnesa Ridge to determine the velocity structure of the contourite sediment away from the influence of the pockmark and the pipe structure beneath it. The other was deployed within the pockmark (Figure 1).

## 4. Data Analysis

### 4.1. CSEM Data Processing

In marine CSEM geophysical measurements, we are interested in the Earth's response to the induced currents due to the electromagnetic source. This response can be represented by a transfer function (TF) and varies according to changes in conductivity, source-receiver offset, and other geometric factors [Myer *et al.*, 2011]. When using a continuous CSEM signal, we examine the infor-

mation about Earth's TF in the frequency domain [Myer *et al.*, 2011]. We have followed the processing method detailed in Myer *et al.* [2011] to analyze the data in frequency domain. We used 1 s analysis window for the Fourier transform of the CSEM data which were then stacked over 60 s windows to improve signal-to-noise (S/N) ratio [Myer *et al.*, 2011]. All the transmitter and receiver navigation (see Appendix A) was merged with the stacked data to assign spatial positions every 46 m along the profile. Due to compass failure in HyBIS, we were unable to obtain directly the orientations of the receiver dipoles, which are important for the quality of 2-D inversion results. The orientation of OBE dipoles was calculated using the orthogonal procrustes rotation analysis (OPRA) code of Key and Lockwood [2010] (Table 1). The angles obtained using OPRA have previously been shown to be accurate to within  $3^\circ$  [Key and Lockwood, 2010]. Data from the top five harmonic frequencies (1–9 Hz) of Vulcan data and top four harmonic frequencies (1–7 Hz) for OBE data were found to have sufficient S/N ratio for detailed analysis. The OBE receivers saturated at amplitudes higher than  $10^{-9}$  V/Am<sup>2</sup>, which usually occurred at source-receiver offsets of around 850 m for the fundamental 1 Hz frequency. The noise floor of the OBE instruments was below  $10^{-12.5}$  V/Am<sup>2</sup>, which at 1 Hz occurred at about 3000 m source-receiver offset. The low-saturation limit and high noise floor are likely to be related to the nature of the preamplifiers used and the age of the Ag-AgCl electrodes used in the OBEs.

### 4.2. CSEM Data Error and Uncertainty

The main sources of error in our data were the location uncertainties for our transmitter antenna and receivers (see Appendix B) and environmental noise (see Appendix C). Due to similarity in the instrument setup to Myer *et al.* [2012], we expected location uncertainties to be the dominant contributor to CSEM data errors. Amplitude and phase uncertainty as a result of location uncertainty in our data were calculated using a composite uncertainty model analysis [Myer *et al.*, 2012]. We then combined the location uncertainty with the environmental noise, captured in our variance calculations, to obtain the total uncertainty for the purpose of CSEM inversion (typically around 2–3% of the datum).

### 4.3. Pseudosection for Vulcan Data

The pseudosection technique is a tool often used in direct current (DC) resistivity and induced polarization (IP) methods as it provides a quick preview of lateral resistivity variations of the subsurface [Weitemeyer *et al.*, 2011]. Weitemeyer *et al.* [2006b] and Weitemeyer and Constable [2010] showed that the same technique can be used to analyze towed receiver (Vulcan) CSEM data. The magnitude of the major axis of the polarization ellipse traced by the electric field ( $P_{\max}$ ) [Smith and Ward, 1974] is a robust way of estimating the horizontal field at the receiver location, as it depends only upon the relative phase between the recorded electric fields and the amplitudes of the horizontal components [Behrens, 2005]. The pseudosection method involves 1-D forward modeling for various resistivity values and computation of polarization ellipses to eliminate source receiver geometry uncertainty in the horizontal plane [Behrens, 2005; Weitemeyer *et al.*, 2006b]. One-dimensional forward models were generated for each transmitter-receiver location for the Vulcan data (Figure 3a) using the Dipole1D forward modeling code of Key [2009]. The 1-D model contained three main

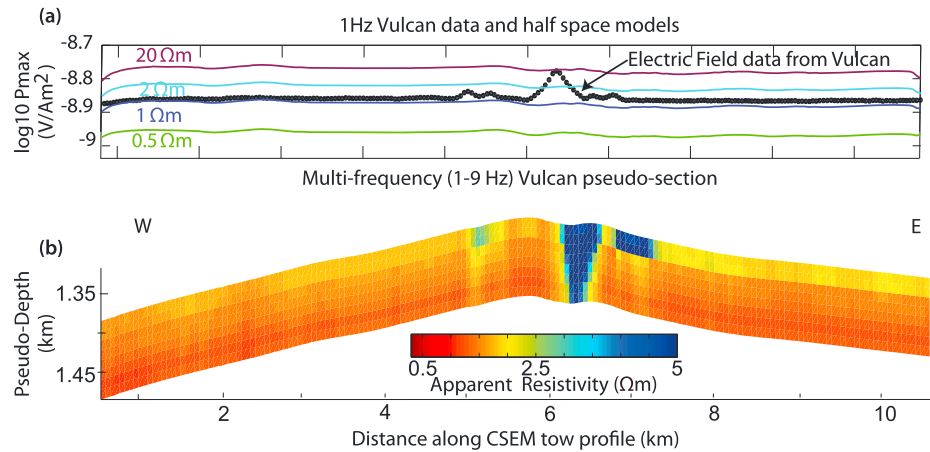


**Figure 3.** (a) One hertz Vulcan data are shown with various 1-D half-space resistivity forward models. (b) Multiple frequency (1–9 Hz) Vulcan pseudosection showing a high resistivity anomaly at the ridge axis and two smaller resistivity anomalies at the ridge flanks. The location of these resistivity anomalies is linked to electric field anomalies ( $P_{\max}$ ) on Vulcan data. Apparent resistivity values for each datum were obtained by searching for the best fitting 1-D half-space resistivity model (computed at 0.1 Ωm intervals) to the observed data.

components: (i) an insulating air layer, (ii) conductive seawater layers with varying conductivity layers recorded by conductivity-temperature-depth (CTD) probe, and (iii) a resistive sediment layer containing a uniform resistivity using a range of resistivity values from 0.3 Ωm to 100 Ωm.

A lookup table method was then used to find an apparent resistivity value for each data point. This involved a search for the resistivity value of the 1-D forward model that gave the best fit to the  $P_{\max}$  value of the data point for each transmitter receiver position [Weitemeyer and Constable, 2010]. The horizontal location of the matching resistivity was assigned to be the midpoint between the transmitter and the receiver. The skin depth of low-frequency CSEM transmission (0.1–10 Hz) is given by  $z_s = 503 \sqrt{\frac{\rho}{f}}$ , where  $f$  is the frequency and  $\rho$  is the resistivity of sediments. We assumed sediment resistivity of 1 Ωm for calculating the skin depth for each frequency. The apparent resistivity value was then assigned to a depth range obtained from the skin depth calculations in decreasing frequency order for each data point.

The apparent resistivity pseudosection for the Vulcan data (Figure 3) shows significant lateral resistivity variation. It shows an anomalous resistive pipe structure at the ridge axis below the pockmark with an apparent resistivity of about 5 Ωm. Two smaller pipe-like features with slightly smaller apparent resistivity anomaly could also be observed on the flanks of the ridge. The apparent resistivity of the smaller pipes is about 2 Ωm which is slightly higher than the background 1.5 Ωm apparent resistivity of the sediments. The magnitude and depth of the anomalies are, however, not useful for any detailed analysis. The Vulcan pseudosection, however, provides better horizontal resolution of shallow resistivity structures than our OBE data which are discussed in section 6.1.

#### 4.4. Inversion of OBE Data

The Vulcan pseudosection gives a useful first look at the lateral subsurface resistivity variation, but inversion of CSEM data is required to obtain a more accurate resistivity image [Weitemeyer et al., 2010]. We used a finite element (FE) forward code, MARE2DEM [Key and Ovall, 2011], that involves a 2.5-D assumption—the Earth is assumed to be invariant in the direction perpendicular to the acquisition direction or inline (2-D Earth), but the 3-D nature of the CSEM source is respected. The code uses unstructured grids of triangular elements to overcome discretization difficulties and to conform readily to complex model features such as topographic variations [Li and Constable, 2007; Li and Pek, 2008; Key and Ovall, 2011]. MARE2DEM implements a nonlinear 2.5-D inversion of CSEM data using a faster implementation of the original Occam code [Constable et al., 1987] to obtain a resistivity image of the subsurface. In our unconstrained application, Occam’s inversion tries to minimize the following regularized function [Constable et al., 1987]:

$$U(\mathbf{m}, \mu) = \|R(\mathbf{m})\|^2 + \mu^{-1} [\|\mathbf{W}(\mathbf{d} - F(\mathbf{m}))\|^2 - \chi_*^2] \quad (1)$$

**Table 2.**  $\chi^2$  Misfit for the 2-D VTI Anisotropic Inversion for Individual OBE Sites and Frequencies<sup>a</sup>

OBE Site	1 Hz	3 Hz	5 Hz	7 Hz
V01	0.60	0.42	0.46	0.51
V02	0.64	0.56	0.61	0.68
V03	0.70	0.61	0.56	0.62
V04	0.76	0.68	0.73	0.79
V05	0.79	0.76	0.77	0.83
V06	0.89	0.76	0.77	0.78
V07	0.84	0.74	0.75	0.80
V08	0.85	0.76	0.69	0.77
V09	0.85	0.64	0.63	0.68
All	0.77	0.68	0.67	0.73

<sup>a</sup>Inversion target misfit of 0.75 was achieved in eight iterations.

where  $\|\cdot\|$  is the Euclidean norm and  $R$ , the measure of roughness, is the discrete first difference operator on the model vector  $\mathbf{m}$  which consists of logarithmic resistivity  $\rho$  values. The first term acts as a regularizer to stabilize the inversion and prevents it from producing wildly oscillating resistivity structures [Constable *et al.*, 1987]. The second term is the measure of the misfit of the forward response  $F(\mathbf{m})$  to the data  $\mathbf{d}$ .  $\mathbf{W}$  is a weighting function that is the inverse of the standard data errors and  $\chi_*^2$  is the target misfit. The result of Occam inversion is mathematically unique because the inversion automatically chooses a value of Lagrange's multiplier,  $\mu$ , in order to fit the smoothest model to the data. In the initial stages of the inversion, it tries to minimize the misfit of the model predictions until it reaches the target misfit. Once the target misfit is reached, it performs a search over a range of  $\mu$  values to find the smoothest model. The unique smooth model is almost independent of the starting model [Wheelock, 2012] in the absence of excessive noise or extreme subsurface resistivity structures.

Two-dimensional inversion of CSEM data requires careful parameterization. Multifrequency (1–7 Hz) OBE amplitude and phase data with transmitter-receiver offsets 850 m to 3000 m were used for the inversion. We specified a simple starting model containing a highly resistive air layer ( $10^{12}\Omega\text{m}$ ), seawater with 10 horizontal resistivity layers (0.295–0.345  $\Omega\text{m}$ ), computed from the recorded CTD measurements during the survey and a constant resistivity of 1  $\Omega\text{m}$  for the sediments below the seafloor. We also specified an accurate seafloor bathymetry, using the sum of the altitude (from altimeter) and depth (from CTD) mounted on the DASI frame. The air and seawater resistivity were fixed while the resistivity below the seafloor is a free parameter in the inversion scheme. Beneath the seabed, the initial triangular mesh were set up such that the mesh became sparser with depth and toward the ends of the profile to minimize computation time. To choose a reasonable target misfit and ensure that the inversion satisfy the global minimum, we ran an initial inversion to an extremely low (0 or 0.1) target misfit, which the inversion could never reach. The target misfit is then found by analyzing the value of misfit and Lagrange's multiplier, and the inversion was rerun with the new target misfit. Both isotropic and anisotropic inversions were initially tested and produced very similar models for the given target misfit and error structures. Since the Occam inversion optimizes the value of Lagrange's multiplier and the roughness term for the given misfit, these parameters are not a good measure of how identical the two models are. Therefore, we refer to the visual similarity of the models. The anisotropic inversion with vertical transverse isotropy (VTI) was, however, smoother in the shallow sediments and converged faster (eight iterations) than the isotropic inversion (14 iterations) and was chosen for our analysis. This inversion reached a target root-mean-square misfit of 0.75 (Table 2) for the given error (approximately 2–3% of the datum).

#### 4.5. OBS Data Analysis

Data from the OBS8 deployed on the flank of the ridge were of high quality, and it was straightforward to pick a series of reflection events extending 700 ms below the seabed at normal incidence (Figure 4a). Picks were made mainly on the hydrophone component. However, the hydrophone was saturated by the shots at short range and the corresponding artifact obscures reflectors within 50 ms of the direct arrival. Therefore, the first reflector below the seabed was picked on the vertical geophone component instead. Pick uncertainties vary from 4–5 ms near the seabed to 8 ms at the deepest reflector. Data from the OBS5 deployed on the pockmark

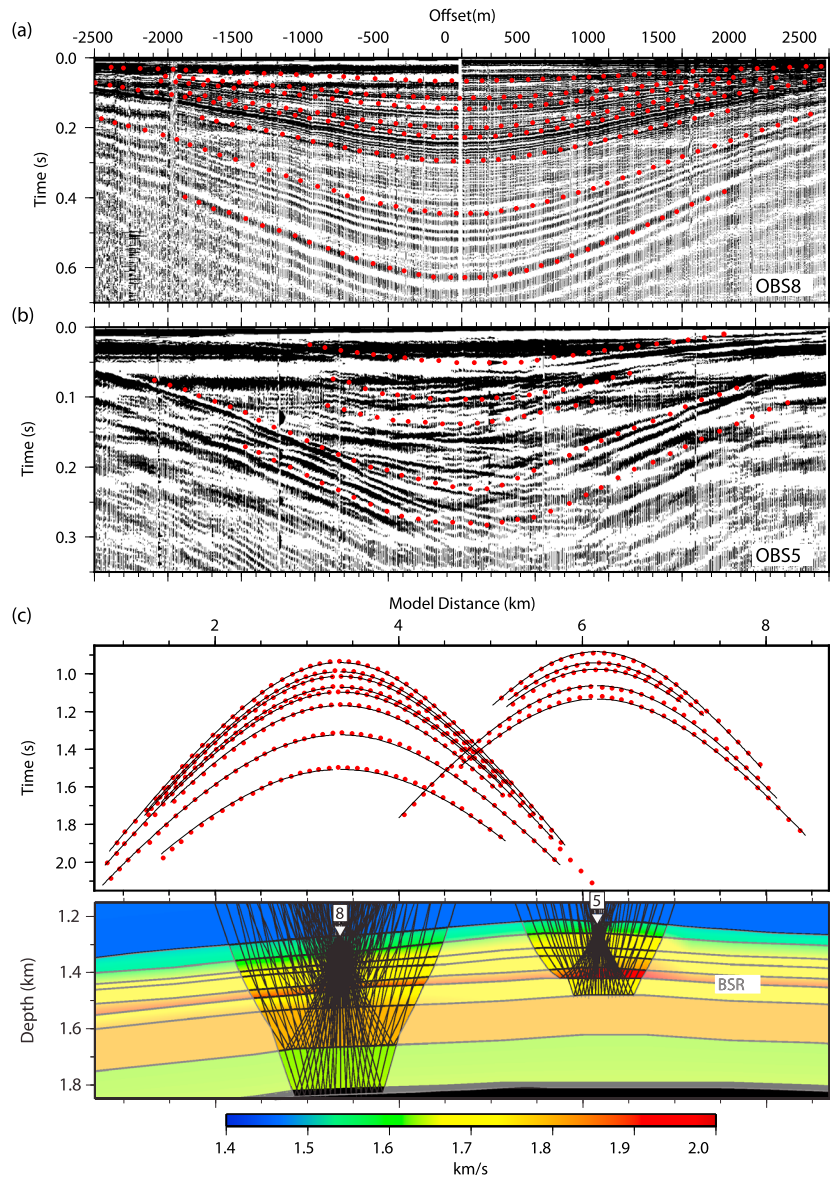


**Figure 4.** (a) Record section from OBS8 on the flank of Vestnesa Ridge. Data were filtered with a trapezoidal band-pass filter with corner frequencies of 10, 20, 250, and 300 Hz and flattened on a direct arrival pick. Hydrophone data are shown at negative offsets and geophone data at positive offsets. Red circles mark every tenth travel time pick. (b) Record section from OBS5 on the pockmark. Processing as for OBS8; hydrophone data only are shown, and red circles mark every tenth travel time pick. (c) Predicted (black lines) and observed (red circles, subsampled as above) travel times for modeled reflectors. (d) Corresponding velocity model. Inverted triangles mark OBS positions, and black lines mark picked reflectors.

were much more difficult to interpret (Figure 4b), but several shallow reflectors could be traced between the two instruments using data from the 60 m streamer. The deepest of these reflectors is the BSR. Some deeper reflectors could also be identified in these data but could not be correlated confidently with reflectors picked on OBS8.

A velocity model was developed using the forward modeling code of Zelt and Smith [1992]. Based on CTD data, the ocean layer was assigned a velocity decreasing linearly from 1.48 km/s at the sea surface to 1.465 km/s at the seabed. Reflector depths were constrained using the coincident reflection profile, and only velocities were adjusted to fit the OBS data. The two OBSs sample the subsurface in a region about 2 km across at the depth of the BSR, so with 3 km between the OBSs, the experiment is not reversed in the classical sense, and a wide range of models could be constructed that would fit the data. Our preferred model (Figure 4d) was developed

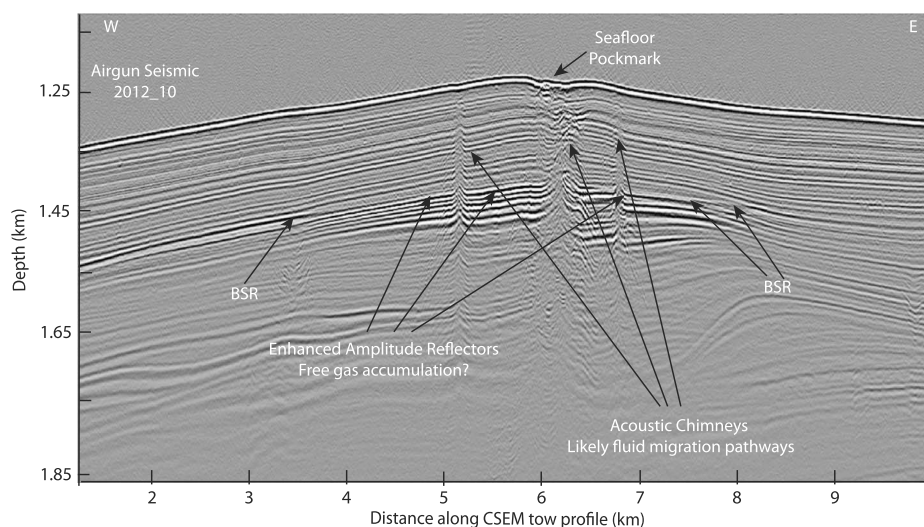


**Figure 5.** The seismic profile 2012\_10 was acquired during the 2012 cruise and shows prominent acoustic signatures of subsurface features at the Vestnesa Ridge. The seismic data were poststack time migrated and have been converted to depth using a 1-D velocity function obtained from the OBS data analysis (Figure 8).

by considering each OBS separately and then merging the models. This model has a root-mean-square misfit of 7 ms and a normalized  $\chi^2$  statistic of 1.485. Given the high quality of the data and pick uncertainties of 1–2% of the two-way time of reflections below the seabed, velocity uncertainties in the vicinity of OBS8 are just a few percent. At OBS5 the uncertainties are larger because of the difficulty of picking reflections.

#### 4.6. Seismic Reflection Data

The seismic reflection data (Figure 5) from the 60-channel streamer were poststack time migrated using a Kirchhoff migration and converted to depth using a simple 1-D variation of velocity with depth below the seabed obtained from the OBS data analysis.

### 5. Synthetic Model Studies of CSEM Data

A resistivity model obtained from the smooth Occam inversion [Constable *et al.*, 1987] usually has poorer resolution compared to seismic velocity models due to the difference in the physics of energy propagation [Constable, 2010]. However, our resistivity model was constrained by nine OBE sites which were approximately 500 m apart, whereas the velocity model was obtained from only two OBS stations that were 3 km apart. We, therefore, expect our resistivity model to have better spatial resolution and coverage than our velocity model. The resistivity model obtained from Occam inversion eliminates spurious features and retains only the essential features that explain the CSEM data [Constable *et al.*, 1987]. The resistivity solution thus obtained is a unique smooth model [Whelock, 2012], but no measure of model uncertainty or resolution is available. We address this issue via synthetic studies.

Inline CSEM data are sensitive to transverse resistance, i.e., the product of resistivity of a feature and its thickness [Constable, 2010]. The resistivity contrast between a resistive feature and the background sediments is therefore an important consideration in trying to answer questions about resolution and sensitivity of our CSEM survey. We want to understand the effect of resistivity contrast and variation in fluid composition on resolution of inverted CSEM data. We have attempted to ensure all parameters in the synthetic inversion resemble the real data in terms of available data, acquisition geometry, S/N ratio, and predicted errors. Gaussian random noise of 2% was added to the synthetic data before inversion. We assumed an ideal scenario where we are able to estimate our errors and specified a 2% data error for the inversion and a target  $\chi^2$  value of 1 which indicates that the model fits the data within their uncertainties. It is, however, likely that the real data have slightly larger uncertainty than we have incorporated in the synthetic data inversions. The synthetic model analysis will therefore provide the best-case scenario of what we can sense and resolve using our CSEM experiment.

We have based our synthetic models primarily on features observed on seismic reflection data (Figure 5). We tested the sensitivity and resolution of a compaction model and various cases of buried resistors. Our assessment of an interpretable anomaly is a resistivity anomaly that has at least the lateral width of two consecutive elements of our initial grid ( $\geq 100$  m) and approximately 0.5  $\Omega\text{m}$  of resistivity contrast.

### 5.1. Model Generation Using Archie's Equation

We assumed a pore-filling scenario and applied a modified version of Archie's equation [Archie, 1942; Winsauer et al., 1952; Hearst et al., 2000] to calculate the approximate subsurface resistivity values for each model. Pore water saturation in sediments can be expressed as

$$S_w = \left[ \frac{\rho_w a \phi^{-m}}{\rho} \right]^{\frac{1}{n}} \quad (2)$$

for pores partially filled with water and hydrate or gas. Here  $S_w$  is sediment water saturation,  $\rho_w$  is the pore water resistivity,  $\rho$  is the measured resistivity of sediments,  $\phi$  is the sediment porosity, and  $n$  is the saturation coefficient, often equal to the cementation constant,  $a$ , and cementation constant,  $m$ , are both related to the interconnection of pores in the sediment matrix. The tortuosity constant was added to the original Archie's equation [Archie, 1942] by Winsauer et al. [1952] and should theoretically be  $a = 1$ . The saturation constant  $n$  was introduced later by Hearst et al. [2000] to account for variation in pore shape, connectivity, and the distribution of the conducting phase.  $S_R$  can easily be calculated from water saturation using

$$S_R = 1 - S_w \quad (3)$$

Since we have no empirical values of Archie's constants for the study area, we used empirical constants from other studies with similar lithologies;  $a = 1$ ,  $m = 2.4$ , and  $n = 2$  [Archie, 1942; Jackson et al., 1978; Evans et al., 1999; Evans, 2007; Schwalenberg et al., 2010; Weitemeyer et al., 2011]. A pore water resistivity trend with depth was obtained using the relationship of Becker [1985]

$$\rho_w = (3 + T/10)^{-1} \quad (4)$$

where  $T$  is the sediment temperature in degrees Celsius obtained using bottom water temperature of  $-0.84^\circ\text{C}$  (obtained from DASI CTD) and a geothermal gradient of 80 C/km [Vanneste et al., 2005; Geissler et al., 2014]. The estimated pore water resistivity trend was similar to the pore water salinity derived pore water resistivity for nearby Ocean Drilling Program (ODP) Site 986 [Jansen et al., 1996]. Sediment resistivities obtained using these assumptions are displayed in Table 3 which show resistivity values for different assumed porosity and pore water saturation which were used for building our synthetic models.

### 5.2. Simple Compaction Model

A resistivity model representing pore water-saturated sediments with decreasing porosity and pore water resistivity with depth (Table 3), similar to ODP Site 986 [Jansen et al., 1996], was first tested (Figure 6a). Limitations of our model-building tool prevented us from specifying smooth changes in porosity, so we defined a five-layer model, which sufficiently accounts for the porosity changes with depth. The inversion converged rapidly (five iterations), and the result shows a strong resemblance to the true model in the overall trend and resistivity values (Figure 6b). Since EM wave propagation at low frequency is diffusive [Constable, 2010], and Occam inversion outputs a smooth model, the inversion result does not contain the sharp resistive boundaries of the true model. Otherwise, the inversion easily recovers the changes in resistivity in the true model down to a depth of about 2.5 km. However, the value of resistivity recovered for the 3  $\Omega\text{m}$  resistor is influenced by the 4  $\Omega\text{m}$  resistivity of the zone beneath.

This observation suggests that we are probably at the limit of resolution of the inversion at the 3–4  $\Omega\text{m}$  boundary. The maximum depth to which our inversion is sensitive, however, is not simple and depends on the available data range, amount of noise, and data errors. An increase in the amount of random noise and specified data uncertainty in inversion parameters both lead to a decrease in sensitivity to the deepest resistivity boundary, and we lose sensitivity to this boundary if noise exceeds 7% of signal in the synthetic inversions.

**Table 3.** Sediment Resistivity for Varying Pore Water Saturation for an Assumed Effective Porosity, and Pore Water Resistivity Trend Similar to Site 986 [Jansen et al., 1996]<sup>a</sup>

Effective Porosity (%)	Pore Water Resistivity ( $\Omega\text{m}$ )	Pore Water Saturation (%)	Resistivity ( $\Omega\text{m}$ )	Assumed Depth (m bsf <sup>b</sup> )
60	0.30	100	1	0–100
		95	1.1	
		90	1.3	
		80	1.6	
		50	4.0	
48	0.26	100	1.5	100–200
		95	1.7	
		90	1.9	
		80	2.4	
		50	6.0	
37	0.19	100	2	200–500
		95	2.3	
		90	2.5	
		80	3.2	
		50	8.2	
26	0.12	100	3	500–1200
		95	3.4	
		90	3.8	
		80	4.8	
		50	12.2	
19.5	0.08	100	4	1200–2200
		95	4.5	
		90	5	
		80	6.3	
		50	16.2	

<sup>a</sup>Resistivity was calculated using Archie's equation [Archie, 1942] for  $a = 1$ ,  $m = 2.4$ , and  $n = 2$ .

<sup>b</sup>Meters below seafloor.

### 5.3. Buried Resistors

#### 5.3.1. Shallow Pipe

An acoustic chimney is observed below the pockmark on seismic reflection data (Figure 5). We designed a 800 m wide and 200 m thick resistive pipe which we expect to resolve if there is sufficient resistivity contrast with the background, as the width of this pipe is more than twice the burial depth [Constable, 2010]. We therefore wanted to test the minimum resistivity contrast within the pipe that we can resolve in the inversion of synthetic data (Figure 6d). Assuming that porosity does not vary laterally, we found that a resistivity contrast equivalent of  $S_R = 5\%$  or higher within the modeled pipe was required to show up as an interpretable anomaly (Figure 6e). The minimum width of a shallow pipe that can be resolved by our inversion was primarily controlled by the size of the meshes used for inversion. We were only able to test and resolve pipe anomalies wider than 100 m, as the minimum side length of our user-defined triangular mesh in the shallow was 50 m. This value was based on the 100 m dipole length and approximately 46 m separation between each stacked datum.

#### 5.3.2. Shallow Resistor

A zone of enhanced amplitude reflectors below the ridge axis can be observed on seismic reflection data around the base of GHSZ (about 200 m beneath the seabed) (Figure 5). Assuming this enhanced reflectivity is due to accumulation of free gas [Hustoft et al., 2009; Bünz et al., 2012], we would also expect a resistive anomaly. Whether the anomaly is resolved by our CSEM experiment depends on the amount of resistive material in the pores. To inform us about the minimum saturation of the resistive material in this zone that we could resolve

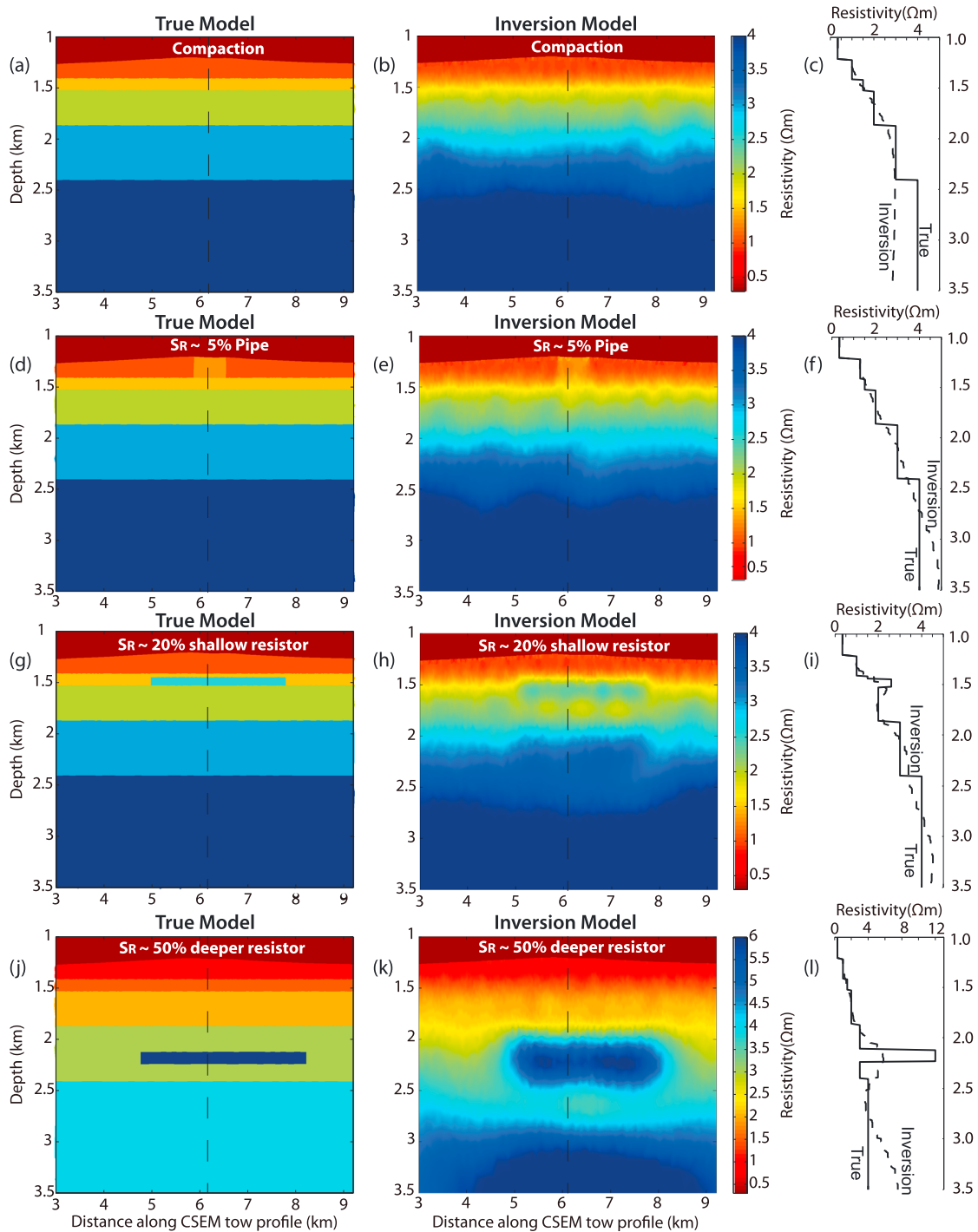


**Figure 6.** Inversion of synthetic CSEM data with identical acquisition geometry, data range, and S/N ratio as acquired data, to test sensitivity and resolution of the inversion for various synthetic models. The synthetic study shows (a and b) a simple compaction model, (d and e) a shallow pipe with resistivity contrast equivalent to  $S_R = 5\%$  resistive material; (g and h) a shallow buried resistor with resistivity contrast equivalent to  $S_R = 20\%$  resistive material, and (j and k) a deep resistor with high resistivity contrast (approximately  $S_R = 50\%$ ) can be resolved by the CSEM inversion. Note that the color scale is different for Figures 6g and 6h. (c, f, i, and l) Resistivity-depth profiles extracted at 6.3 km model distance (dashed line) are also displayed to the right of each inversion model for each synthetic test. The comparison between true and inverted models demonstrates that the inversion almost recovers the transverse resistance for each synthetic case study.

with our CSEM survey, we generated synthetic models in which a 3 km wide and 80 m thick zone 200 m below the ridge axis had  $S_R$  values of 2%, 5%, 10%, 20%, and 50% (Figure 6g).

The inverted resistivity of the various scenarios suggests that although  $S_R = 10\%$  shows up as a slight anomaly on the inversion results, it will be hard to interpret the result without prior knowledge of the true model.  $S_R = 20\%$  was inferred to be the lower limit for our CSEM survey to resolve confidently (Figure 6h). Although we are able to resolve this  $S_R = 20\%$  resistive anomaly, the dimensions of the resistor are different from the true model. There is also an effect on the resistivity of the deeper 3  $\Omega\text{m}$  resistor due to a possible trade-off between the thickness and resistivity of the zone, as CSEM data are sensitive to transverse resistance. For a 1-D resistivity profile extracted at 6.3 km model distance (Figure 6i), the transverse resistance of 208  $\Omega\text{m}^2$  for the 80 m thick (1450–1530 m), 2.6  $\Omega\text{m}$  resistor of the true model was recovered by the CSEM inversion as a 100 m thick (1440–1540 m) resistor with resistivity ranging in 1.8–2.3  $\Omega\text{m}$ .

### 5.3.3. Deeper Resistor

We would like to determine whether there is any deep gas reservoir feeding the observed fluid escape features on seismic reflection data. The maximum resolvable depth of the CSEM inversion is around 2.5 km (about 1 km beneath the seabed) (Figure 6b). We therefore wanted to see whether we can resolve the top and the base of a 120 m thick deep resistive feature of 12  $\Omega\text{m}$  at a depth of approximately 2.2 km (Figure 6j).

We found that a very high resistivity contrast was required for the inversion to resolve such a deep resistor; e.g., our  $S_R = 50\%$  saturation model. The true resistivity anomaly modeled was 12  $\Omega\text{m}$  extended from 4.5 to 8.2 km along the profile and was 120 m thick. The inverted resistivity anomaly was about 2–3 times (240–360 m) the original thickness and slightly shorter (around 500 m) with lower resistivities between 4 and 6  $\Omega\text{m}$  in magnitude. The inverted deep resistive anomaly also distorted the deeper layers of the model and introduced a deep terminating layer. The CSEM inversion is at the limits of its sensitivity at the center of our deep synthetic anomaly around 2.2 km. It therefore fails to fully resolve the base of the deep anomaly as well as the deeper resistive boundary underneath the anomaly as it tries to find a trade-off between resistivity and thickness to account for the anomaly in the synthetic data (Figure 6k). The transverse resistance of 1440  $\Omega\text{m}^2$  (120 m  $\times$  12  $\Omega\text{m}$ ) for the deep resistor between 2120 and 2240 m was recovered as 1426  $\Omega\text{m}^2$  by integrating the transverse resistance between 1980 and 2260 m (280 m thick) which had resistivities between 3.7 and 5.9  $\Omega\text{m}$  (Figure 6l). The transverse resistance of the inverted model for the deep resistor was within 1% of the true model.

## 6. Result

### 6.1. Two-Dimensional Inversion

The resistivity models obtained from the isotropic inversion (Figure 7a) and VTI anisotropic inversion (Figures 7b to 7d) of OBE data were very similar, with the vertical resistivity model (Figure 7b) being smoother for the shallow sediments. Very weak anisotropy within the shallow sediments (Figure 7d) was predicted by the anisotropic inversion. However, in deep water setting like our survey (>1200 m), inline data are primarily sensitive to vertical resistivity [Ramananjaona et al., 2011; MacGregor and Tomlinson, 2014]. Additionally, MacGregor and Tomlinson [2014] and Ramananjaona et al. [2011] also showed that broadside data are required to have improved sensitivity to the horizontal resistivity in deep waters. However, for our data, between the offsets (850–3000 m) and frequencies (1–7 Hz) used in our inversion, inline data could have some sensitivity to horizontal resistivity as well [MacGregor and Tomlinson, 2014]. Since only inline data were available for our inversion and the vertical and horizontal resistivity models were very similar, we will focus on the vertical resistivity results in this paper. The main features of the vertical resistivity model are discussed below.

#### 6.1.1. Central Resistive Pipe

A high-resistivity zone can be observed beneath the seafloor pockmark from 6.1 to 6.6 km along the resistivity profile, coinciding with the pipe structures imaged in the seismic reflection profile (Figure 7b). This zone extends from the seafloor to a depth of about 300 m below the pockmark. It has slightly higher resistivity value toward the center, which increases in magnitude to the seafloor. The resistivity ranges from about 2.5  $\Omega\text{m}$  at the edges to about 4  $\Omega\text{m}$  at center in the lower part of the pipe whereas the central part of the anomaly is about 6  $\Omega\text{m}$  just below the pockmark location. The feature is also connected to a deeper zone of high resistivity via an extension of the elevated resistivity pipe of about 2.25  $\Omega\text{m}$  magnitude. The core of the higher resistivity appears to be located around 5–7 km along the profile at the depth of about 2.3 km below the sea surface (approximately 1.3 km below seafloor) with a maximum resistivity of approximately 3  $\Omega\text{m}$ .

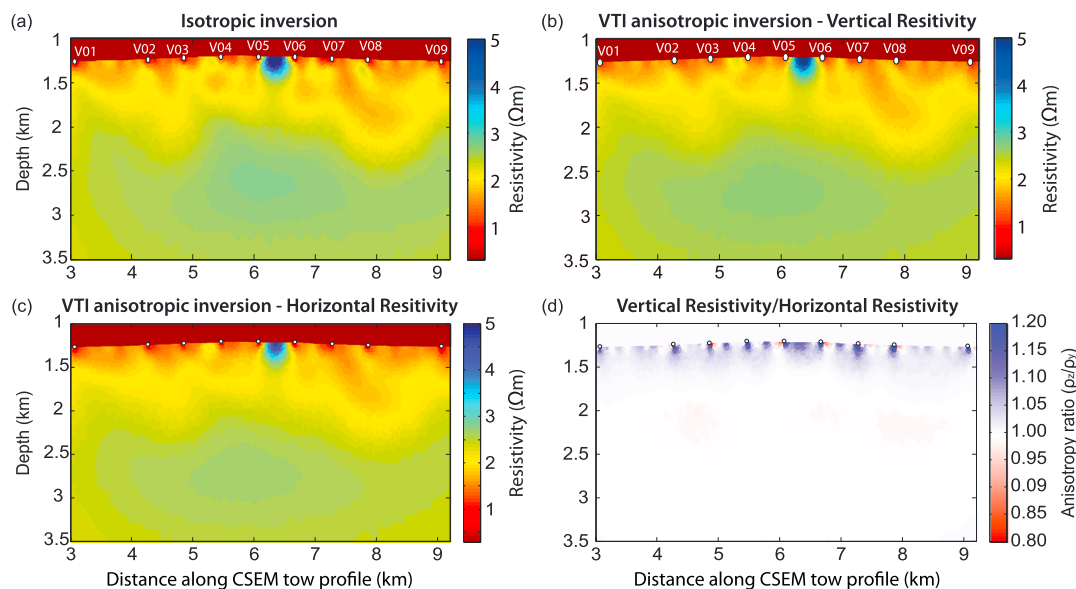


**Figure 7.** Resistivity models obtained from 2.5-D inversion of OBE data. (a) Isotropic inversion was initially tested and shows a similar result to the anisotropic inversions. The isotropic inversion reached the target misfit of 0.75 in 14 iterations. (b) The vertical resistivity model obtained from the VTI anisotropic inversion results are, however, smoother just beneath the seafloor and was therefore chosen as the preferred result for interpretation. The anisotropic inversion reached the target misfit of 0.75 in eight iterations. (c) The horizontal resistivity model also shows lateral resistivity variation with a prominent central chimney structure with a zone of high resistivity at depth. (d) The ratio of vertical to horizontal resistivity reveals weak anisotropy in the shallow sediments.

**6.1.2. Narrow Elevated Resistive Zones at Ridge Flanks**

A few regions of higher resistivity connected to the deep resistive anomaly can be observed on both flanks of the ridge (Figure 7b). These features of about 2.25 Ωm and sometimes can be observed to reach close to the seafloor, such as at around 5 and 7 km along the model distance (Figure 7b).

**6.2. Velocity Models**

At OBS8, the model shows velocities increasing with depth from 1.51 km/s at the seabed to 1.88 km/s at the BSR, then a decrease to 1.70 km/s, with anomalously low velocities then present to the bottom of the model

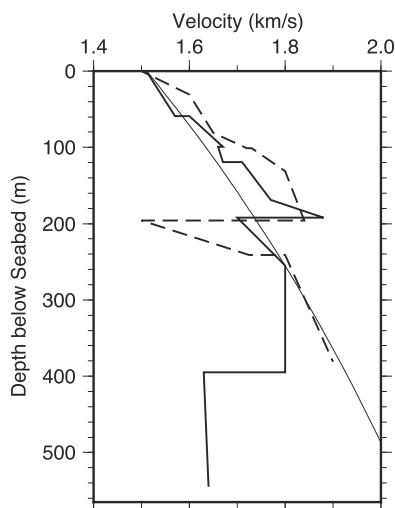


**Figure 8.** Solid line marks velocity at the location of OBS8. Dashed line marks velocity at site N3 of Chabert et al. [2011]. Thin curve marks Hamilton's [1980] regression for terrigenous sediments.

(Figures 4d and 8). The model includes lateral velocity variations in all the layers, but an adequate fit to the data can be achieved if such variations are restricted to the layer immediately above the BSR. Larger lateral variations in the shallower layers are also allowed by the data from OBS5, and such variations might not be sampled by OBS8 since reflection points for shallow reflectors are very close to the OBS.

The lateral velocity increase can be attributed to the presence of hydrate beneath the pockmark, but its magnitude is not sufficiently constrained to allow an estimate of hydrate saturation based on these data alone. The spatial coverage of the velocity model (Figure 4d) is limited by the number of OBS stations and their large separation (approximately 3 km).

**7. Discussion**

Reliable coincident seismic and resistivity models are limited to a small area (Figure 9a) due to large spacing (approximately 3 km) between the two OBSs and extend only up to a depth of 1850 m, which limits the maximum depth of our joint interpretation. A low-velocity zone can be associated with the

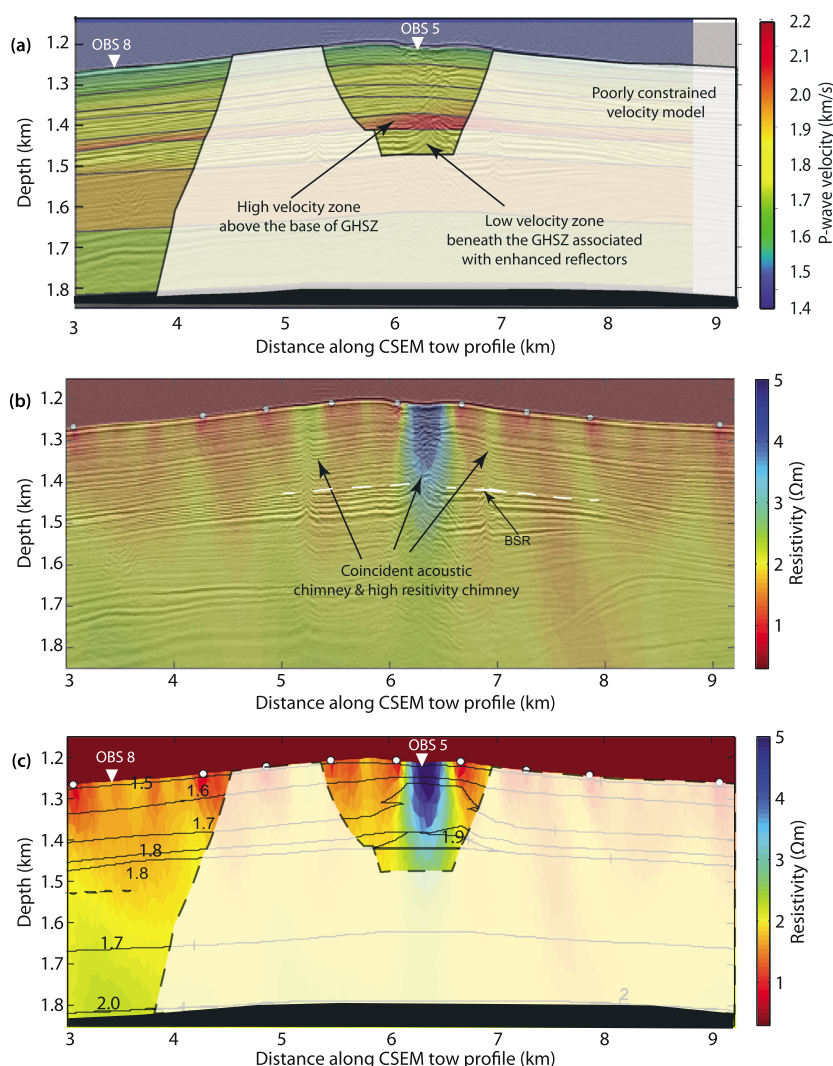


**Figure 9.** (a) Seismic velocity and seismic reflection data overlay shows a low-velocity zone associated with the enhanced reflectors beneath the GHSZ. (b) Vertical resistivity and seismic reflection data overlay shows a high correlation between the resistive chimney and the acoustic chimney. The seismic fluid escape features on the ridge flanks are also associated with higher resistivity anomalies. No strong resistivity anomaly can be observed with the high-amplitude reflectors beneath the BSR. (c) Velocity contours overlaid on resistivity results show an increase in seismic velocity toward the lateral position of the resistive chimney. There is no clear resistivity anomaly associated with the low-velocity zone beneath the BSR at the ridge axis suggesting a very low concentration of free gas.

enhanced amplitude reflectors beneath the GHSZ with lower apparent frequency (Figure 9a). The frequency loss and enhanced amplitudes can be caused by the presence of gas [Hustoft *et al.*, 2007]. The low-velocity zone suggests the presence of a free gas zone (FGZ) at least 50 m thick below the ridge axis. The FGZ may extend at least 300 m below the BSR (Figure 8), but its thickness is not constrained by our OBS data on the ridge axis.

The zone directly above the FGZ has high velocity (Figure 9a). In order to assess the presence of velocity (and resistivity) anomalies due to the presence of hydrate or gas, we must establish a reference background velocity function that we expect in the absence of either.

**7.1. Velocity Anomaly**

The appropriate background velocity for hemipelagic sediments in this region was investigated extensively by Westbrook *et al.* [2008], using differential effective medium (DEM) models. They concluded that two alternative models (their DEM2 and DEM3) were most appropriate, and these models both predict a very similar velocity-depth function to the empirical curve of Hamilton [1980] (Figure 8). We constructed velocity anomaly

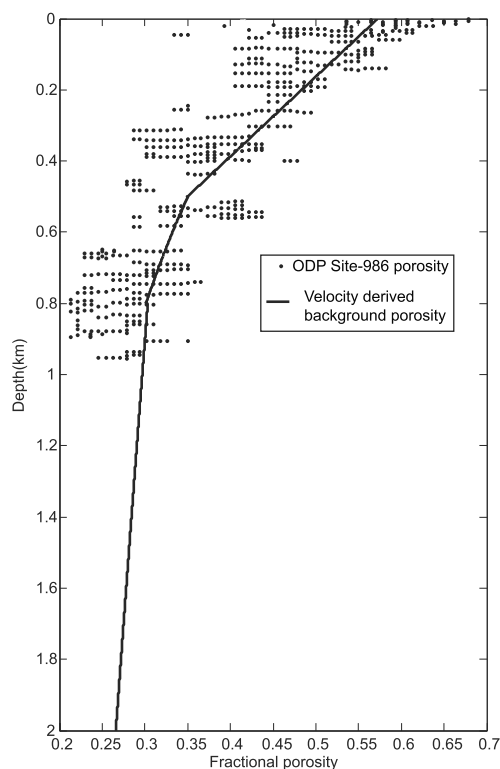


**Figure 10.** Background porosity estimate for the study obtained using a reference velocity function. The reference velocity function consists of *Hamilton's* [1980] curve for terrigenous sediments for the top 800 m bsf and *Ritzmann's* [2004] velocity trend below. It was converted to density and porosity using *Hamilton's* [1978] regression equations. A different velocity-density equation (equation (4)) was used for the unconsolidated sediments ( $\leq 2$  km/s). Archie's equation [Archie, 1942] (empirical constants  $a = 1$ ,  $m = 2.4$ , and  $n = 2$ ) was used to convert the reference porosity function into a background resistivity function.

plots using DEM2, DEM3, and Hamilton's curve as reference velocity, and all looked very similar; therefore, we have used the Hamilton's curve here (Figure 11a).

We observe a positive velocity anomaly above the BSR associated with our high-velocity zone and a negative velocity anomaly associated with the underlying FGZ (Figure 11a). Similar observations of high-velocity anomalies above the BSR and low-velocity anomalies beneath have been reported due to gas hydrate near our study area, on the West Svalbard margin [Westbrook et al., 2008; Hustoft et al., 2009; Chabert et al., 2011] and on the mid-Norwegian Atlantic margin [Bünz, 2004; Hustoft et al., 2007; Plaza-Faverola et al., 2010].

### 7.2. Resistivity Anomaly

In the absence of hydrate or gas, the seismic velocity response in the subsurface is largely controlled by changes in porosity whereas resistivity changes can be caused by changes in either porosity or fluid composition. Assuming water-saturated pores, we used the reference background velocity trend to calculate a reference background porosity trend (Figure 10). First, we extended the reference velocity function beyond 1 km depth below the seabed, where the comparisons of Westbrook et al. [2008] are no longer valid, by using the velocity trend of Ritzmann et al. [2004]. Initially, we used Hamilton's [1978] velocity-density relationship to convert the reference velocity function to a reference density function. However, we found that Hamilton's [1978] relationship for unconsolidated sediments (velocity  $< 2$  km/s) provided a poor fit to the density log from nearby ODP Site 986 [Jansen et al., 1996] which likely sampled similar lithologies. Therefore, we used an altered equation for the unconsolidated sediments which provided a good fit to density and porosity data from Site 986 (Figure 10).

$$d = 0.743V + 0.602 \tag{5}$$

Here  $d$  is the density and  $V$  is the  $P$  wave velocity of sediments. The altered equation also provided a better fit than Hamilton's [1978] relationship to the Site 986 density log when we used both relationships to convert the ODP velocity log to density. We used a grain density of  $2710 \text{ kg/m}^3$  and pore water density of  $1023.7 \text{ kg/m}^3$  [Jansen et al., 1996] to obtain a reference porosity trend. Comparison of our reference velocity to the ODP Site 986 velocity log suggests approximately 4% uncertainty in our reference velocity function within the top 1000 m bsf. We infer approximately 5% uncertainty in our estimated density obtained using equation (5) by comparison with the Site 986 density log and 6–8% uncertainty in our inferred porosity trend.

The background resistivity trend was then estimated using Archie's equation [Archie, 1942] using  $a = 1$  and  $n = 2$  and  $m = 2.4$ , which fits the ODP Site 986 resistivity log. The pore water resistivity trend was derived for the synthetic models and matches the trend suggested by ODP Site 986 salinity [Jansen et al., 1996]. The resistivity anomaly (Figure 11b) was calculated by comparing the vertical resistivity model (Figure 7b) with the reference background resistivity model. Reference resistivity obtained from porosity using equation (2) also suggested a reasonable fit to the ODP Site 986 resistivity log for  $m = 2.2$ – $2.6$ . Accounting an uncertainty of 10% for Archie's constant  $m$  and 10–15% for the geothermal gradient [Vanneste et al., 2005] in equation (4), roughly 18–20% ambiguity is likely for our reference resistivity trend.

A resistivity anomaly straddling the BSR (Figure 11b) can be associated with the velocity anomalies (Figure 11a) beneath the ridge axis. This display highlights strong anomalies around the chimney structures which extends beneath the BSR at the central chimney. The FGZ beneath the ridge axis could be a possible explanation for the observed negative velocity anomaly and positive resistivity anomaly beneath the BSR, but the positive resistivity anomaly could also be a smoothing artifact of the CSEM inversion. A joint saturation estimate is therefore not appropriate. Away from the chimney, the free gas saturation immediately below the BSR is likely to be on the lower end of that predicted at site N3 [Chabert *et al.*, 2011] as indicated by the less pronounced low-velocity zone (Figure 8).

There is no strong resistivity anomaly within the GHSZ away from the chimneys, which suggests low hydrate saturations that may not be detectable our survey setup. Hustoft *et al.* [2009] suggest around 10% hydrate saturation near the base of the GHSZ and around 2% free gas saturation beneath, which is too low to be resolved by our CSEM survey according to our synthetic model studies. A deeper resistivity anomaly can also be identified (Figure 11b), which could be caused by widespread presence of free gas beneath the GHSZ with a possible free gas reservoir at depth. At this depth, our data are mainly sensitive to the transverse resistance (Figure 6h) which makes it difficult to perform a saturation analysis.

### 7.3. Apparent Porosity Anomaly

One common parameter that links resistivity and velocity of sediments is porosity. The velocity and resistivity models were converted into apparent porosity models using methods described earlier and compared to the reference background porosity (Figure 10) function to obtain apparent porosity anomalies. The positive velocity anomalies above the BSR (Figure 11a) correspond to lower apparent porosity (Figure 11c), and the negative velocity anomalies beneath the BSR (Figure 11a) correspond to higher apparent porosity (Figure 11c). On the other hand, from resistivity models, we obtain a lower apparent porosity anomalies both above and beneath the BSR (Figure 11d) since both hydrate and gas show up as positive resistivity anomaly (Figure 11b).

### 7.4. Chimney Structures

The central chimney beneath the pockmark is 500–600 m wide whereas the chimneys on the ridge flanks are narrower (100–120 m) with lower resistivity (Figure 9b). The disturbed sequence of reflectors within the acoustic chimneys, and the associated high resistivity extend beyond the FGZ beneath the BSR (Figure 9b). This observation could suggest a deeper source of fluid migration into the GHSZ.

Geochemical analysis of samples taken at the pockmark above the central chimney suggests episodic release of thermogenic gas through the chimney for over 20 ka [Panieri *et al.*, 2014; Smith *et al.*, 2014a]. The central chimney is therefore likely a long-term feature with three-phase equilibrium for gas, hydrate, and water extending throughout the GHSZ [Liu and Flemings, 2007; Smith *et al.*, 2014b]. We therefore expect both gas and hydrate to coexist within the chimney.

Free gas migration through the long-term chimney is likely to occur through microfractures and faults [Smith *et al.*, 2014b] which are not resolved by our seismic reflection data. However, the enhanced reflectors associated with the FGZ beneath the central chimney have a small vertical offset between the eastern and the western ridge flank, which is an argument for possible faulting within the central chimney. Microfractures and faults within a fluid escape chimney with similar sediments have been suggested at the Nyegga CNE03 pockmark [Plaza-Faverola *et al.*, 2010].

### 7.5. Free Gas and Hydrate Saturation Estimates Within the GHSZ

By including both resistivity and velocity information in rock physics models, we can constrain both free gas and hydrate saturations within the GHSZ. Our pore water-saturated background velocity and resistivity models were based on ODP Site 986 [Jansen *et al.*, 1996] and may not be accurate as this site is around 200 km away from our study area. Therefore, for quantitative saturation estimates, we computed a depth-integrated, average velocity and resistivity for the top (0–100 m bsf) and bottom (100 m bsf to BSR) parts of the GHSZ for every 50 m along our profile (Figures 11e and 11f). This approach has the additional benefit of reducing the amount of scatter in our cross plots when comparing our data to predicted resistivity and velocity models. The observed depth-integrated average velocity for the top (Figure 11e) and bottom (Figure 11f) parts of the chimney was around 5% and 8% higher than the background, respectively. The observed depth-integrated average velocity outside the chimney was similar to the background for the top part of the GHSZ (Figure 11e) and around 2% higher for the bottom part of the GHSZ (Figure 11f). In addition to the velocity anomalies, the observed depth-integrated average resistivities within the central chimney were 15–380% and 30–180%

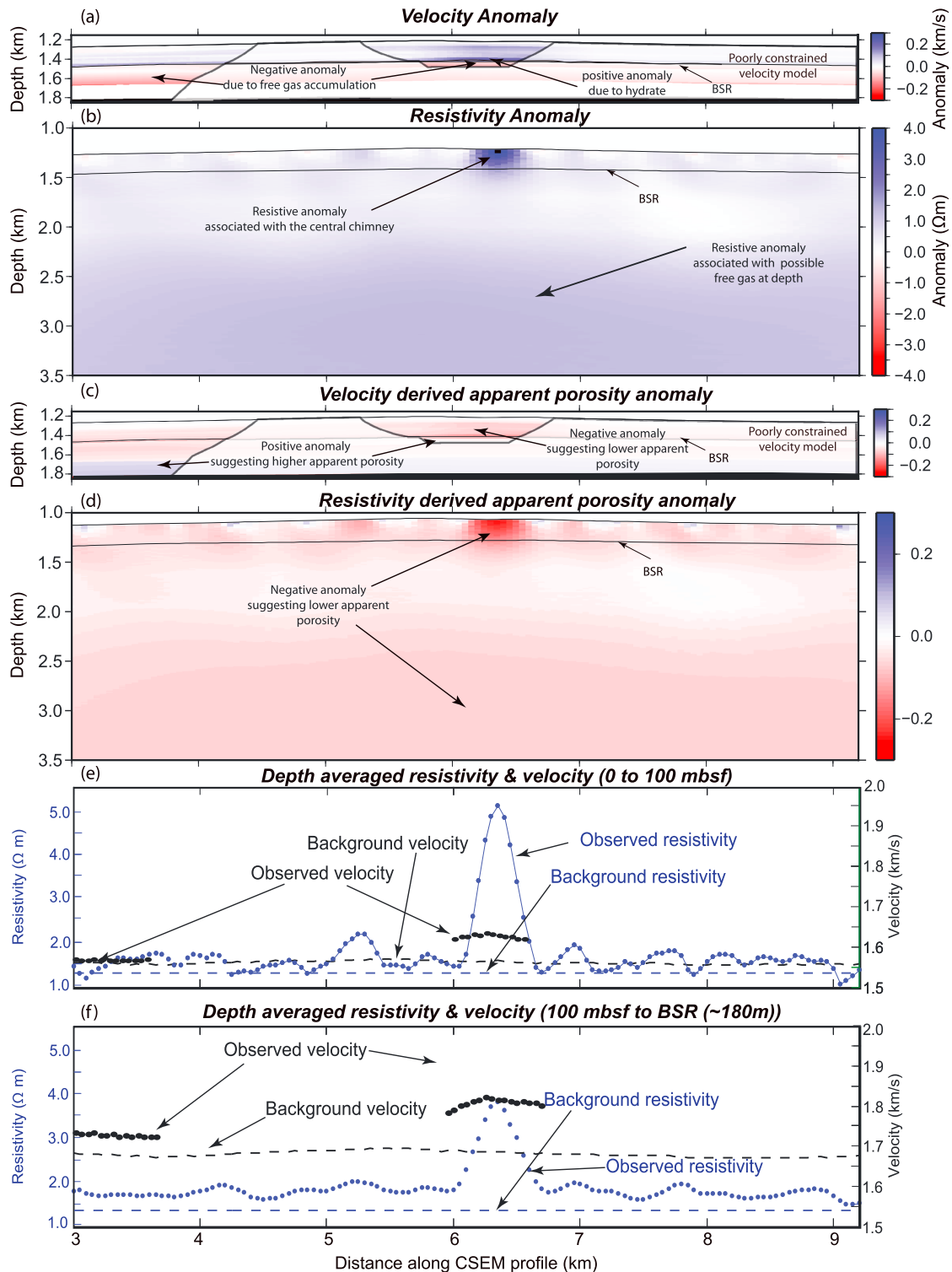


**Figure 11.** (a) Velocity anomaly showing the difference between the observed velocity model and a water-saturated background velocity obtained from the *Hamilton* [1980] curve for terrigenous sediments. A positive anomaly within the GHSZ and a negative anomaly beneath the GHSZ can be observed clearly. (b) Resistivity anomaly showing the difference between the observed resistivity and background resistivity generated from velocity-derived porosity (Figure 10) highlights anomalies associated with the chimney structures and at depth. (c) Apparent porosity anomaly derived from the velocity model showing a region of lower apparent porosity above the BSR and higher apparent porosity below the BSR. (d) Apparent porosity anomaly derived from the resistivity model showing a region of lower apparent porosity associated with the chimney structures beneath the GHSZ. Depth-averaged velocity and resistivity comparison for the (e) top part and (f) bottom part of the GHSZ along the CSEM profile showing the locations of the highest anomalies. A coincident positive resistivity and positive velocity anomaly can be observed around the central chimney.

higher than the background for the top (Figure 11e) and bottom (Figure 11f) parts, respectively. Outside the central chimney, the depth-integrated average resistivities for the top (Figure 11e) and bottom (Figure 11f) parts of the GHSZ were 0–300% and 30–300% higher than the background, respectively. To quantify the amount of hydrate and free gas saturation within the top and bottom parts of the GHSZ, we replaced the pore water in our background models by varying amounts of hydrate and gas to estimate the theoretical velocity and resistivity responses.

#### 7.5.1. Velocity Models

We used two different rock physics models for calculating the velocity response due to change in pore fluid saturation: fracture-filling model of *Plaza-Faverola et al.* [2010] and Gassman's fluid substitution [*Berryman, 1999*].

1. We used the simple fracture-filling model of *Plaza-Faverola et al.* [2010] as our preferred model for estimating the velocity response due to varying hydrate saturation within the pores. In this model, free gas replaces pore fluids, and hydrate formation from this gas leads to a change in porosity of the original frame. This model, however, only accounts for hydrate as fraction of volume and was not useful for modeling the effect of free gas.
2. To estimate the velocity response for both free gas and hydrate in pores, we adapted Gassman's fluid substitution [*Berryman, 1999*] to account for hydrate in the rock frame (see Appendix D). The velocity response obtained from Gassman's substitution [*Berryman, 1999*] is strongly influenced by the mixing model used to calculate the bulk modulus of the fluid mixture. The Reuss and Voigt bounds provide the lower and upper bound for the bulk modulus, respectively. The Reuss bound is expected to provide an accurate estimate of bulk moduli of the fluid mixture when the constituents are liquids or gases [*Mavko et al., 2009*] which leads to a uniform mixture. The effect of nonuniform distribution was modeled by using the Voigt-Reuss-Hill average [*Mavko et al., 2009*].

#### 7.5.2. Resistivity Model

Since we do not have direct measurements of the electrical properties of the various minerals, we used Archie's equation [*Archie, 1942*] for our resistivity calculations. A depth-averaged pore fluid resistivity, a depth-averaged GHSZ porosity, and other empirical constants as used for the background resistivity calculations were assumed. The bulk modulus estimated using Reuss bound and resistivity obtained from Archie's equation are consistent in the assumption of a uniform fluid distribution (Figures 12a and 12b).

#### 7.5.3. Saturation Estimate for Central Chimney

Estimated saturations depend on whether a uniform (Reuss bound) or a nonuniform (Reuss-Voigt-Hill average) fluid distribution is assumed within the pores. Inferred hydrate and free gas saturations for the top (Figures 12a and 12b) and bottom (Figures 12c and 12d) parts of the chimney for each of the mixing models are listed in Table 4.

Assuming a nonuniform fluid distribution, up to 22% free gas saturation is inferred at the top part of the chimney (Figure 12b). As the distribution of gas that has migrated through the chimney is likely to be patchy, the nonuniform model (Figures 12b and 12d) is better suited for predicting the effect of the gas on seismic velocity. So the larger concentrations of gas and smaller concentrations of hydrate predicted from this model, compared with those from the uniform model, are more probable. This high free gas saturation may result in high pore fluid pressures that could push fluids, including free gas, to the seafloor [*Westbrook et al., 2009*].

In the absence of direct sampling of hydrate and gas from deep boreholes in the study area, the inferred hydrate, and gas saturation for the chimney can be compared with those modeled for the postbreaching case (20 ka) of a long-term chimney by *Smith et al.* [2014b] where 50–80% hydrate and up to 1% free gas saturation was predicted in the top 200 m. Our saturation estimates are therefore comparable to the model chimney [*Smith et al., 2014b*] for hydrates but higher for free higher saturation. The model chimney is in similar water depths but has a thicker GHSZ and higher temperature and salinity profiles. The 20 ka postbreaching model of *Smith et al.* [2014b] suggests highest hydrate and gas saturation directly beneath the seafloor, consistent with the location of the highest resistivity observed in our model (Figure 9b).

Although we infer the greatest amount of resistive material at the top part of our studied chimney, the hydrate saturation is estimated to be slightly higher at the bottom part of the chimney in the case of our nonuniform fluid distribution, which contrasts with *Smith et al.*'s [2014b] model. It is difficult to determine the cause of the difference between the model chimney and our observations in the absence of temperature and salinity measurements from the Vestnesa chimney. If, however, an average salinity of 85 parts per thousand (ppt) and 65 ppt was assumed for the top and bottom parts of our chimney, respectively, based on the salinity profile of

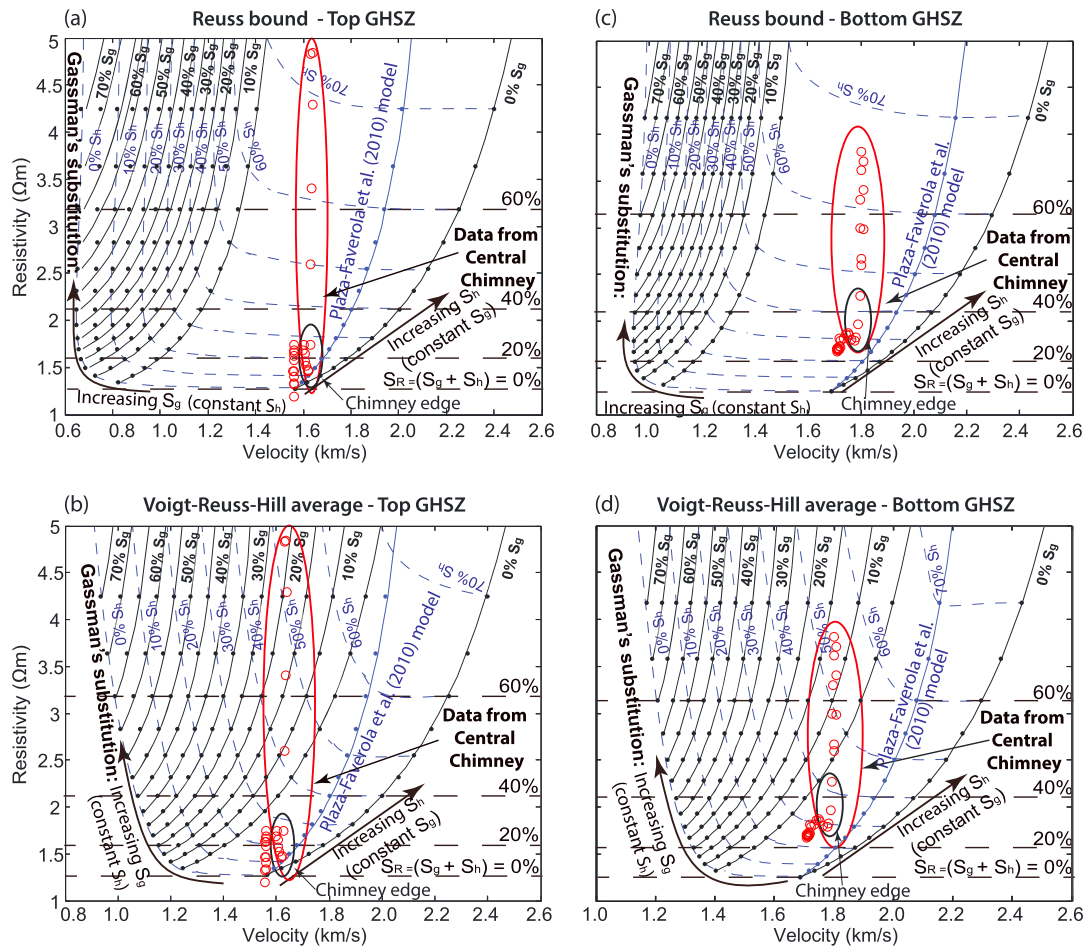


**Figure 12.** Cross plot showing depth-averaged velocity and resistivity for the GHSZ (also see Figures 11e and 11f) against theoretical models. The resistivity is calculated using Archie's equation [Archie, 1942], whereas two different models were used for the velocity: (a)  $\phi = 55\%$ , (c)  $\rho_w = 0.303 \Omega\text{m}$  and (b)  $\phi = 50.5\%$ , (d)  $\rho_w = 0.243 \Omega\text{m}$ . The Plaza-Faverola et al. [2010] model (solid blue line in each panel) assumes that hydrate is formed as free gas flows into fractures and veins and alters the porosity of the frame. This model is only valid in the absence of free gas. To model free gas along with hydrate, Gassman's substitution [Berryman, 1999] was used for each load-bearing hydrate frame. The bulk modulus of the gas and pore water mixture was calculated using the Reuss bound (Figures 12a and 12b) and the Voigt-Reuss-Hill average (Figures 12c and 12d) to explore the different fluid mixing scenarios. The noncircled datum represents the region outside the chimney.

Smith et al. [2014b], the estimated pore water resistivity using the equation of state of Lewis and Perkin [1981] would be  $0.10 \Omega\text{m}$  and  $0.14 \Omega\text{m}$ , respectively. These pore water resistivity values are much lower compared to  $0.30 \Omega\text{m}$  (32 ppt) for the top and  $0.24 \Omega\text{m}$  (30 ppt) for the bottom parts of the chimney estimated for our area on the basis of the bottom water temperatures and geothermal gradients (see section 5.1). The amount of hydrate and gas would then be higher in the top part of the chimney for both uniform and nonuniform fluid distribution (Figure E1 in Appendix E). The location of the highest saturation at the top of the chimney is then consistent with the model of Smith et al. [2014b].

#### 7.5.4. Saturation Estimate Outside Central Chimney

Our resistivity and velocity cross plots suggest the presence of up to 30% hydrate saturation in the top part and 20–30% in the bottom part of the GHSZ. Both uniform and nonuniform fluid distribution models suggest less than 5% free gas saturation for the GHSZ with a slightly higher value for the nonuniform model. Whether we assume the uniform distribution (Reuss bound) or nonuniform distribution (Voigt-Reuss-Hill average), the predicted hydrate saturation outside the chimney (Table 4) is higher than previous estimates of 11% for the Vestnesa Ridge [Hustoft et al., 2009]. These predictions are closer to those from the frame-plus-pore model of Westbrook et al. [2008], for their NW Svalbard study location, where 5–25% hydrate in pore space was predicted using a reference velocity from Hamilton [1978]. Our higher hydrate saturation estimates outside the chimney arise from the constraints provided by the resistivity data which allow us to take account of the effect of free gas on velocity within the GHSZ.

**Table 4.** Inferred Hydrate and Gas Saturation (% of Pore Space) for the Central Chimney Obtained Using Joint Resistivity and Velocity Analysis (Figure 12)<sup>a</sup>

Location	Uniform Hydrate	(Reuss) Gas	Patchy Hydrate	(Voigt) Gas
<i>Chimney Top (0–100 m bsf)</i>				
Edge	10–30	<1	10–30	0–2
Center	50–73	1–4	40–52	10–22
Outside	0–30	0–1	0–25	0–4
<i>Bottom (100 m bsf—BSR)</i>				
Edge	30–45	<1	30–42	0–5
Center	50–68	0–2	40–55	5–15
Outside	20–30	0–1	20–30	1–3

<sup>a</sup>Approximately  $\pm 25\%$  uncertainty is estimates for these inferred saturations.

### 7.5.5. Saturation Uncertainties

Our inferred saturations have large uncertainties due to assumptions made while choosing the background functions and using ODP Site 986 for reference, which is approximately 200 km away. An additional complication for our models is that the host sediments are clay rich which is not accounted for by the modified Archie's equation (equation (2)) [Archie, 1942]. The effect of clay conductivity and cation exchange capacity [Waxman and Smits, 1968; Revil et al., 1998] is therefore ignored in our estimates, which likely leads to an overestimate of pore water saturations ( $S_w$ ). This will lead to an underestimate of hydrate and gas saturations. In addition, hydrate is likely to form in fractures in low permeability clay-rich sediments [Liu and Flemings, 2007], which our resistivity models do not incorporate.

Perturbation analysis allows us to obtain a first-order estimate of our inferred saturation uncertainties. It is our preferred approach due to the nonlinearity in the relationship between velocity, resistivity, and saturation presented in our cross plots (Figure 12). On the basis of analysis of the ODP Site 986 logs, around 4% uncertainty in our reference velocity and around 10% in our choice of Archie's parameter  $m$  were inferred. The uncertainty in our reference velocity leads to around 8% uncertainty in our reference porosity used for the saturation estimates. Although the depth-averaging approach reduces these uncertainties slightly, we consider the higher values for our analysis to compensate for the poor controls on our parameter assumptions. The perturbation analysis for  $m$  and porosity suggests up to 18% uncertainty in our inferred saturations of gas and hydrate for both uniform and nonuniform gas distributions. On the other hand, the uncertainty in inferred saturation is around 20% due to the difference in assumption of uniform and nonuniform gas distribution models. We therefore assume 20% (larger of the two estimates) as the saturation uncertainty due to ambiguity in the estimated theoretical velocity and resistivity responses. However, no measure of uncertainty in our resistivity data is known. Occam inversion [Constable et al., 1987] only outputs a smooth resistivity model and does not provide any measure of model uncertainty. Postcalculation of model uncertainty by perturbing the final model is not practical due to large compute times (current inversion takes approximately 24 h on 64 nodes of 4x Xeon E5/Core i7 1333 MHz processors with 256GB RAM) as this would require several inversions to perform this analysis. However, we can infer an uncertainty of 10% in our depth-averaged resistivity and velocity data. This may account for an additional 5% saturation uncertainty. Accounting for the largest errors in the theoretical and observed values, we suggest around 20–25% uncertainty in our inferred saturations obtained from our cross plots.

The inferred values of hydrate and free gas saturation are high for normal values of salinity and even higher for the values of salinity predicted by Smith et al. [2014b]. The absence of particularly high or low values of seismic velocity is a consequence of the presence of free gas and hydrate together, probably as a consequence of locally high pore water salinity caused by the formation of hydrate, which suppresses the conversion of the remaining gas to hydrate. Additionally, the presence of authigenic carbonate, formed by anaerobic oxidation of methane, at shallow depth, would with its high seismic velocity counteract the effect of gas on average velocity. As carbonate also has a high resistivity, it cannot be distinguished from hydrate, using our data, so it is probable that in the shallowest part of the chimney, where carbonate is most likely to be abundant, the amount of hydrate is overestimated.

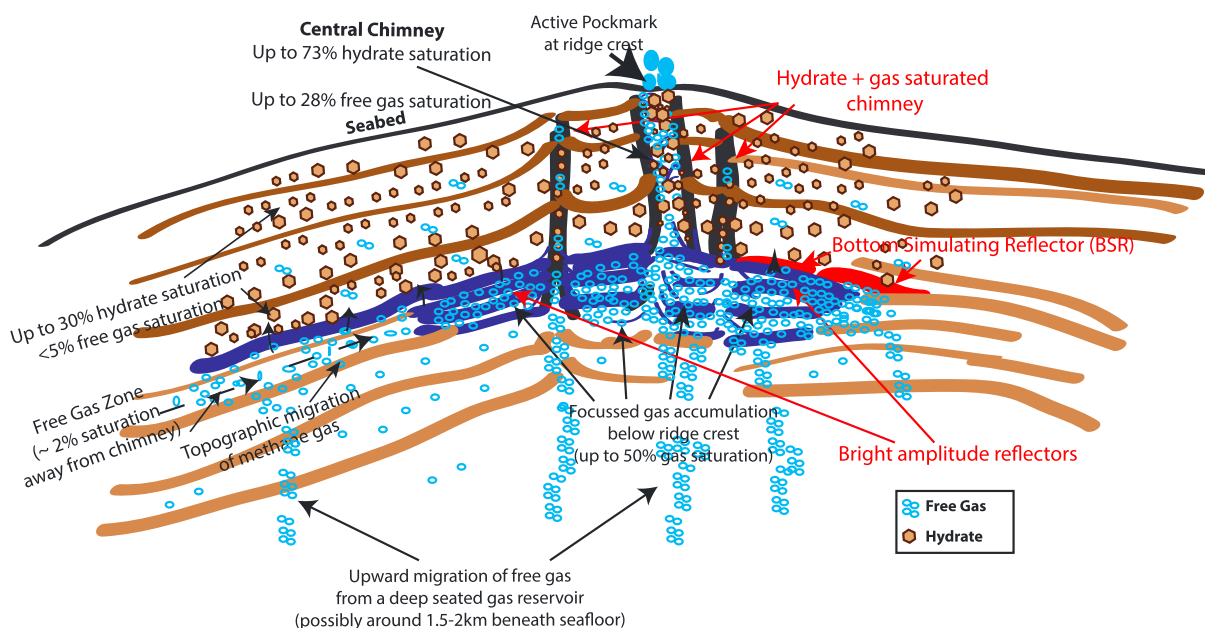


**Figure 13.** A schematic cartoon of the gas hydrate system at the Vestnesa Ridge on the basis of collocated seismic and CSEM data. A GHSZ with up to 30% hydrate saturation is inferred within the GHSZ on the basis of coincident seismic and resistivity data. Extremely high hydrate and free gas saturation is inferred within the chimney beneath the pockmark at the ridge axis where active venting was observed in 2008 [Westbrook *et al.*, 2009]. A FGZ with around 2% free gas saturation is inferred beneath the GHSZ which is likely to be overpressured beneath the ridge axis [Hustoft *et al.*, 2009]. Up to 50% free gas saturation may be inferred directly beneath the chimney using our resistivity estimates. There is also evidence of the FGZ being fed by a deeper gas reservoir.

The presence of hydrate, carbonate, and free gas with high contrasts of acoustic impedance between them and the normal sediment, and the acoustic absorption caused by free gas would lead to significant attenuation of seismic waves traveling through a volume of sediment that was heavily invaded by them. Strong seismic attenuation beneath the pockmark, however, is not shown above the BSR by seismic reflection sections, except very locally, although the gas-invaded region beneath the BSR shows strong attenuation (Figure 5). Furthermore, at the seabed, emissions of gas bubbles into the water are confined to a few small seep sites around the periphery of the pockmark. From these observations, we infer that although high salinity water is likely to be present locally in and around active gas-migration pathways, it is probably not characteristic of the whole of the chimney volume.

## 8. Conclusion

We were able to constrain the degree of hydrate and free gas saturation within the GHSZ at the Vestnesa Ridge (Figure 13) for the first time, using joint velocity and resistivity analysis from coincident seismic and CSEM data. Although it is difficult to judge the accuracy of these estimates, Gao *et al.* [2012] showed that joint seismic and resistivity estimates provide better constraints on porosity and fluid saturation compared to estimates using seismic and EM data individually. From these estimates, we conclude that

1. The top part of the chimney (0–100 m bsf) beneath the pockmark is likely to be highly saturated by hydrate and gas. Maximum depth-averaged saturations of 73% hydrate and 4% free gas or 52% hydrate and 22% free gas are possible assuming uniform and nonuniform fluid distribution, respectively.
2. In the bottom part of the chimney (100 m bsf—BSR), a maximum depth-averaged saturation of 68% hydrate and 2% free gas or 55% hydrate and 15% free gas are possible assuming uniform and nonuniform fluid distribution, respectively.
3. Up to 25% hydrate and 2% free gas might be present in the GHSZ outside the central chimney, with highest hydrate saturation in the bottom part of the GHSZ.
4. The amount of gas estimated in the top part of the chimney makes it very likely to be overpressured, resulting in free gas being expelled through the seafloor.
5. Widespread existence of free gas beneath the GHSZ can be inferred, with a possible free gas reservoir at depth feeding the GHSZ. New CSEM and seismic surveys that have an increased depth of investigation would be required to resolve fully the size and nature of the deep gas reservoir.

Although there is a need for boreholes into the pockmark and the ridge flank to test our interpretations, we have been able to demonstrate that CSEM is a good complement to other geophysical methods for resolving issues of fluid saturation in complex geological settings, such as the Vestnesa pockmark.

### Appendix A: Navigation

Accurate navigation is essential for improvement in quality of quantitative interpretation using CSEM data [Morten *et al.*, 2009; Constable, 2010; Weitemeyer and Constable, 2014]. Ambiguity in antenna dip and cross-line uncertainty as a result of feather has large impact on the quality of CSEM inversion [Weitemeyer and Constable, 2014]. The GPS provided the ship's position that was then used as an input to the USBL navigation system to obtain the position of the towed instrument, DASI frame, and HyBIS. The course over ground (COG) of the DASI frame was calculated using the vector given by the instantaneous position of the ship and the DASI frame. We assumed that Vulcan followed the DASI track. The positions of the DASI and Vulcan antennae were then calculated by back projecting the DASI frame coordinates using the COG and laybacks (Figure 2). Uncertainties in position resulting from this approach would affect the accuracy of our CSEM models and were taken into consideration in CSEM inversion parameterization (see section 4.2).

### Appendix B: Location Uncertainty

The ship's position obtained from the GPS, which was used by the USBL for the position of the deep towed DASI frame and HyBIS (for OBE deployments), had a horizontal uncertainty of  $\pm 4$  m. The USBL system was calibrated during the 2012 cruise and was found to be accurate to 0.1% of slant range. During CSEM operation, the ship maintained a steady course and sailed in an almost straight line. Considering the amount of cable ( $> 1500$  m) and the weight of the towed equipment—DASI frame, DASI streamer, and Vulcan—we expected them to follow the ship's track. However, it was found that the position of the DASI frame shifted from slightly north of the ship track to slightly south of the ship track around the crest of the Vestnesa Ridge. This could be due to deepwater currents on the flanks of the ridge.

Although the neutrally buoyant oil-filled streamer used for the DASI antenna was expected to keep it horizontal, uncertainty existed over its dip during periods when the length of the tow cable was altered to maintain a constant height of DASI 50 m above the seabed. The dip and azimuth of the DASI antenna could also have been affected by the positive buoyancy of Vulcan, attached to the tail of the antenna by a tow rope. Near-bottom currents could also influence the position of DASI antenna and Vulcan. An approximate uncertainty of  $\pm 2$ – $3^\circ$  on antenna dip was assumed on the basis of observed jitter on DASI height and changes in bathymetry. We also assumed a  $\pm 2$ – $3^\circ$  uncertainty in the calculated azimuth of the towed antenna and Vulcan, on the basis of observed jitter in the position of ship and DASI. This orientation uncertainty leads to a  $\pm 7$  m uncertainty for the DASI antenna-middle position, a  $\pm 5$  m uncertainty in the DASI antenna-middle depth, and about  $\pm 12$  m uncertainty on the position of Vulcan. The OBE receivers, which were deployed using HyBIS, also had a  $\pm 6$  m position uncertainty, on the basis of GPS uncertainty and USBL uncertainty.

### Appendix C: Environmental Uncertainty

There were a number of other possible causes of error in our data, such as currents and acoustic interference, which we grouped as environmental noise. These sources caused a certain amount of instability to our receivers during operation and resulted in noise appearing in our data. Stacking of the data into 60 s windows provided us with a measure of variance (typically  $< 1.5\%$  of the datum) in our data along with an improvement in S/N ratio.

### Appendix D: Estimating Velocity Due to Both Free Gas and Hydrate

The reference background  $P$  wave velocity and background porosity trends for the study area were presented in sections 7.1 and 7.2. The shear wave velocity trend was calculated using Castagna's (1985) mudrock relation [Mavko *et al.*, 2009]. These background trends were then used to calculate the depth-integrated background porosity ( $\phi$ ),  $P$  wave velocity ( $v_p$ ), and  $S$  wave velocity ( $v_s$ ) for the top (0–100 m bsf) and bottom (101 m bsf to BSR) parts of the GHSZ. The bulk modulus ( $K$ ), shear modulus ( $\mu$ ), and density ( $d$ ) of hydrate (hyd), gas (g), water (water), and sediment grains (grain) used for the calculations were based on ODP Site 986 (Appendix D and Table D1) [Jansen *et al.*, 1996; Carcione *et al.*, 2005]. The density of the top and bottom parts of the GHSZ was then calculated from

$$d_{\text{GHSZ}} = (\phi)d_{\text{water}} + (1 - \phi)d_{\text{grain}} \quad (\text{D1})$$

**Table D1.** Material Properties for the Svalbard Area as Suggested by *Carcione et al.* [2005]

Material	Bulk Modulus ( $K$ (GPa))	Shear Modulus ( $\mu$ (GPa))	Density ( $d$ (kg/m <sup>3</sup> ))
Grain	29.8	18.0	2623
Hydrate	7.7	3.2	910
Free Gas	21		130
Water	2.24		1024

The bulk and shear modulus of the water-saturated sediments were estimated using equations (D2) and (D3).

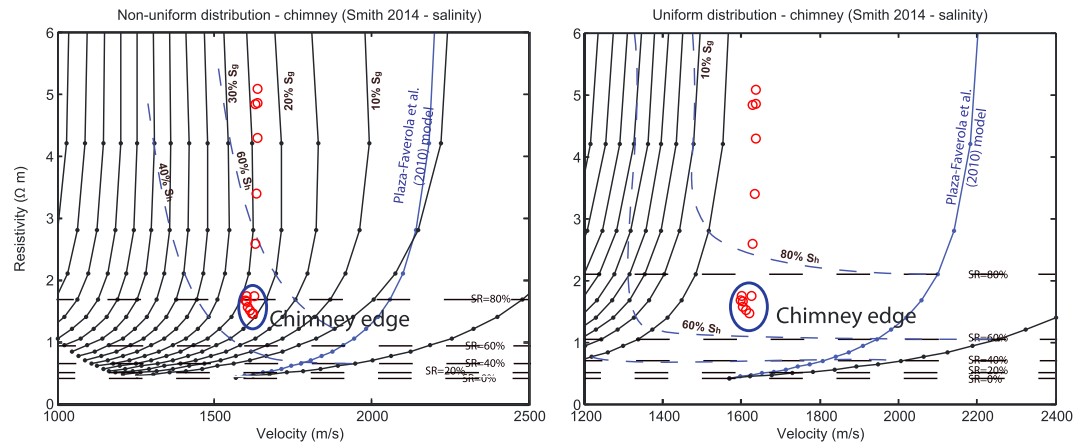
$$\mu_{\text{satGHSZ}} = (v_s^2)d_{\text{GHSZ}} \tag{D2}$$

$$K_{\text{satGHSZ}} = (v_p^2 - \frac{4}{3}v_s^2)d_{\text{GHSZ}} \tag{D3}$$

The dry bulk modulus of the frame was then estimated by solving Gassman's equation which simplifies to

$$K_{\text{dryGHSZ}} = \frac{\frac{K_{\text{satGHSZ}}(\phi)}{K_{\text{water}}} + \frac{K_{\text{satGHSZ}}(1-\phi)}{K_{\text{grain}}}}{\frac{(1-\phi)}{K_{\text{grain}}} - \frac{2}{K_{\text{grain}}} + \frac{K_{\text{satGHSZ}}}{K_{\text{grain}}^2}} \tag{D4}$$

**TOP Chimney (0-100mbsf), Salinity 85ppt, Pore-fluid resistivity - 0.10  $\Omega$ m**



**BOTTOM Chimney (100 mbsf - BSR), Salinity 65ppt, Pore-fluid resistivity - 0.14  $\Omega$ m**

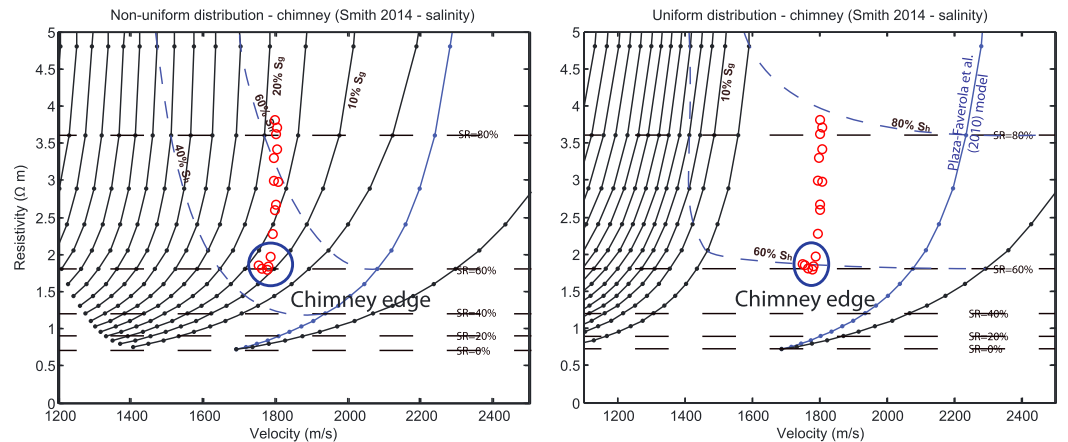


**Figure E1.** Cross plot showing the depth-averaged observed velocity and resistivity data from the top and bottom parts of the central chimney, along with theoretical estimates of velocity and resistivity assuming depth-averaged salinity values from the postbreaching behavior of a long-term chimney suggested by *Smith et al.* [2014b]. The theoretical estimates for velocity and resistivity are estimated in the same way as Figure 12.

Assuming a certain saturation of hydrate ( $S_{\text{hyd}}$ ) within the pores, the fraction of hydrate ( $F_{\text{hyd}}$ ), grain ( $F_{\text{grain}}$ ), and water ( $F_{\text{water}}$ ) in the sediments can be easily calculated using mixing laws. Hydrate formation was assumed to reduce the porosity of the GHSZ and alter the bulk and shear modulus of the new frame containing hydrate and rock.

$$\phi_{\text{frame}} = \phi - F_{\text{hyd}} \quad (\text{D5})$$

The dry modulus of the new dry frame, mineral frame, and the shear modulus of the new mineral frame containing hydrate and rock was then estimated using a Reuss-Voigt-Hill average.

We then replaced pore water by varying the saturation of free gas and computed the bulk modulus of the new pore fluid composition using the Reuss bound and a Reuss-Voigt-Hill average. The shear modulus of the new composition was assumed to be same as the dry case and used to compute the  $P$  wave velocity response.

### Appendix E: Figure-Cross Plot Assuming *Smith et al.* [2014b] Salinity

Figure E1 shows a cross plot of the depth-averaged observed velocity and resistivity data from the top and bottom parts of the central chimney, along with theoretical estimates of velocity and resistivity assuming depth-averaged salinity values from the postbreaching behavior of a long-term chimney suggested by *Smith et al.* [2014b].

#### Acknowledgments

We are grateful to the captain, crew, and shipboard scientific party of RRS James Clark Ross cruises JCR269A and JCR269B for their hardwork at sea. We are also thankful to Veit Huehnerbach for operating HyBIS, Laurence North, Hector Marin-Moreno, and Yee Yuan Tan for their time during DASI operation and PhD students, Amelia Astley, Anupama Rajan, Carolyn Graves, Helen Miller, and Joan Campanya i Llovet for their hardwork during the two cruises. We would also like to thank Natural Environment Research Council's Ocean Bottom Instrumentation Facility and especially Ben Pittcairn and Robert Kirk for their onboard technical support. This research would not have been possible without the funding of the National Environment Research Council (NERC), UK (grants NE/H002732/1 and NE/H022260/1). Seismic and CSEM data are archived at the British Oceanographic Data Centre (email: enquiries@bodc.ac.uk). We would also like to thank Kerry Key for developing the MARE2DEM code and making it publicly available and David Myer for the CSEM processing codes and valuable discussions. We would like to thank the two anonymous reviewers for their comments and feedback which helped to improve the quality of this paper.

#### References

- Archie, G. E. (1942), The electrical resistivity log as an aid in determining some reservoir characteristics, *Trans. Am. Inst. Min. Eng.*, *146*, 54–62.
- Becker, K. (1985), Large scale electrical resistivity and bulk porosity of the oceanic crust, deep sea drilling project hole 504B, Tech. Rep., Initial Report, Deep Sea Drilling Project, doi:10.2973/dsdp.proc.83.124.1985.
- Behrens, J. P. (2005), The detection of electrical anisotropy in 35 Ma Pacific lithosphere: Results from a marine controlled-source electromagnetic survey and implications for hydration of the upper mantle, PhD thesis, Univ. of Calif., San Diego.
- Berryman, J. G. (1999), Origin of Gassmann's equations, *Geophysics*, *64*(5), 1627–1629, doi:10.1190/1.1444667.
- Bünz, S. (2004), Acoustic imaging of gas hydrate and free gas at the Storegga Slide, *J. Geophys. Res.*, *109*, B04102, doi:10.1029/2003JB002863.
- Bünz, S., S. Polyanov, S. Vadakkepullyambatta, C. Consolaro, and J. Mienert (2012), Active gas venting through hydrate-bearing sediments on the Vestnesa Ridge, offshore W-Svalbard, *Mar. Geol.*, *332*–334, 189–197, doi:10.1016/j.margeo.2012.09.012.
- Carcione, J. M., D. Gei, G. Rossi, and G. Madrussani (2005), Estimation of gas-hydrate concentration and free-gas saturation at the Norwegian-Svalbard continental margin, *Geophys. Prospect.*, *53*(6), 803–810, doi:10.1111/j.1365-2478.2005.00502.x.
- Chabert, A., T. A. Minshull, G. K. Westbrook, C. Berndt, K. E. Thatcher, and S. Sarkar (2011), Characterization of a stratigraphically constrained gas hydrate system along the western continental margin of Svalbard from ocean bottom seismometer data, *J. Geophys. Res.*, *116*, B12102, doi:10.1029/2011JB008211.
- Collett, T. S., and J. Ladd (2000), Detection of gas hydrate with downhole logs and assessment of gas hydrate concentrations (saturation) and gas volumes on the Blake Ridge with electrical resistivity data, in *Proceedings of the Ocean Drilling Program, Scientific Results*, vol. 164, edited by C. K. Paull et al., pp. 179–191, Ocean Drilling Program, College Station, Tex.
- Collett, T. S., M. W. Lee, M. V. Zyrianova, S. A. Mrozewski, G. Guerin, A. E. Cook, and D. S. Goldberg (2012), Gulf of Mexico Gas Hydrate Joint Industry Project Leg II logging-while-drilling data acquisition and analysis, *Mar. Pet. Geol.*, *34*(1), 41–61, doi:10.1016/j.marpetgeo.2011.08.003.
- Constable, S. (2010), Ten years of marine CSEM for hydrocarbon exploration, *Geophysics*, *75*(5), 75A67–75A81.
- Constable, S. C., R. L. Parker, and G. Constable (1987), Occam's inversion: A practical algorithm for generating smooth models from electromagnetic sounding data, *Geophysics*, *52*(3), 289–300.
- de Boye Montegut, C., G. Madec, A. S. Fischer, A. Lazar, and D. Iudicone (2004), Mixed layer depth over the global ocean: An examination of profile data and a profile-based climatology, *J. Geophys. Res.*, *109*, C12003, doi:10.1029/2004JC002378.
- Edwards, R. N. (1997), On the resource evaluation of marine gas hydrate deposits using sea-floor transient electric dipole-dipole methods, *Geophysics*, *62*(1), 63–74.
- Eiken, O., and K. Hinz (1993), Contourites in the Fram Strait, *Sediment. Geol.*, *82*(1–4), 15–32, doi:10.1016/0037-0738(93)90110-Q.
- Ellis, M., R. Evans, D. Hutchinson, P. Hart, J. Gardner, and R. Hagen (2008), Electromagnetic surveying of seafloor mounds in the northern Gulf of Mexico, *Mar. Pet. Geol.*, *25*(9), 960–968, doi:10.1016/j.marpetgeo.2007.12.006.
- Engen, O., J. I. Faleide, and T. K. Dyreng (2008), Opening of the Fram Strait gateway: A review of plate tectonic constraints, *Tectonophysics*, *450*(1–4), 51–69, doi:10.1016/j.tecto.2008.01.002.
- Evans, R. L. (2007), Using controlled source electromagnetics to map the shallow section of seafloor: From the coastline to the edges of the continental slope, *Geophysics*, *72*, WA105–WA116.
- Evans, R. L., L. K. Law, B. St. Louis, S. Cheesman, and K. Sananikone (1999), The shallow porosity structure of the Eel shelf, northern California: Results of a towed electromagnetic survey, *Mar. Geol.*, *154*(1–4), 211–226, doi:10.1016/S0025-3227(98)00114-5.
- Fisher, R. E., et al. (2011), Arctic methane sources: Isotopic evidence for atmospheric inputs, *Geophys. Res. Lett.*, *38*, L21803, doi:10.1029/2011GL049319.
- Forsberg, C. F., A. Solheim, E. Jansen, and E. S. Andersen (1999), The Depositional Environment of the Western Svalbard Margin During the Late Pliocene and the Pleistocene: Sedimentary facies at Site 986, in *Proceedings of the Ocean Drilling Program, Scientific Results*, vol. 162, edited by M. E. Raymo et al., pp. 233–246, Ocean Drilling Program, College Station, Tex.
- Gao, G., A. Abubakar, and T. M. Habashy (2012), Joint petrophysical inversion of electromagnetic and full-waveform seismic data, *Geophysics*, *77*(3), WA3–WA18.
- Gay, A., M. Lopez, P. Cochonat, D. Levaché, G. Sermondadaz, and M. Seranne (2006), Evidences of early to late fluid migration from an upper Miocene turbiditic channel revealed by 3D seismic coupled to geochemical sampling within seafloor pockmarks, Lower Congo Basin, *Mar. Pet. Geol.*, *23*(3), 387–399, doi:10.1016/j.marpetgeo.2006.02.004.

- Gebhardt, A., W. Geissler, J. Matthiessen, and W. Jokat (2014), Changes in current patterns in the Fram Strait at the Pliocene/Pleistocene boundary, *Quat. Sci. Rev.*, 92, 179–189, doi:10.1016/j.quascirev.2013.07.015.
- Geissler, W. H., P. V. Pulm, W. Jokat, and A. C. Gebhardt (2014), Indications for the occurrence of gas hydrates in the fram strait from heat flow and multichannel seismic reflection data, *J. Geol. Res.*, 2014, 582424, doi:10.1155/2014/582424.
- Haacke, R. R., G. K. Westbrook, and R. D. Hyndman (2007), Gas hydrate, fluid flow and free gas: Formation of the bottom-simulating reflector, *Earth Planet. Sci. Lett.*, 261(3–4), 407–420, doi:10.1016/j.epsl.2007.07.008.
- Hamilton, E. L. (1980), Geoacoustic modeling of the sea floor, *J. Acoust. Soc. Am.*, 68(5), 1313–1340.
- Hamilton, L. (1978), Sound velocity-density rocks relations in sea-floor sediments and rocks, *J. Acoust. Soc. Am.*, 63(2), 366–377.
- Hearst, J. R., P. H. Nelson, and F. L. Paillet (2000), *Well Logging for Physical Properties*, 2nd ed, John Wiley, Hoboken, N. J.
- Howe, J. A., T. M. Shimmield, and R. Harland (2008), Late quaternary contourites and glaciomarine sedimentation in the fram strait, *Sedimentology*, 55, 179–200, doi:10.1111/j.1365-3091.2007.00897.x.
- Hustoft, S., J. Mienert, S. Bünz, and H. Nouzé (2007), High-resolution 3D-seismic data indicate focussed fluid migration pathways above polygonal fault systems of the mid-Norwegian margin, *Mar. Geol.*, 245(1–4), 89–106, doi:10.1016/j.margeo.2007.07.004.
- Hustoft, S., S. Bünz, J. Mienert, and S. Chand (2009), Gas hydrate reservoir and active methane-venting province in sediments on <20 Ma young oceanic crust in the Fram Strait, offshore NW-Svalbard, *Earth Planet. Sci. Lett.*, 284(1–2), 12–24, doi:10.1016/j.epsl.2009.03.038.
- Jackson, P. D., D. Taylor Smith, and P. N. Stanford (1978), Resistivity-porosity-particle shape relationships for marine sands, *Geophysics*, 43(6), 1250–1268.
- Jakobsson, M., R. Macnab, L. Mayer, R. Anderson, M. Edwards, J. Hatzky, H. W. Schenke, and P. Johnson (2008), An improved bathymetric portrayal of the Arctic Ocean: Implications for ocean modeling and geological, geophysical and oceanographic analyses, *Geophys. Res. Lett.*, 35, L07602, doi:10.1029/2008GL035250.
- Jansen, E., M. Raymo, and P. Blum (1996), Shipboard Scientific Party 2 Hole 986A, in *Proceedings of the Ocean Drilling Program, Initial Reports*, vol. 162, pp. 287–342, Ocean Drilling Program, College Station, Tex.
- Key, K. (2009), 1D inversion of multicomponent, multifrequency marine CSEM data: Methodology and synthetic studies for resolving thin resistive layers, *Geophysics*, 74(2), F9–F20.
- Key, K., and A. Lockwood (2010), Determining the orientation of marine CSEM receivers using orthogonal Procrustes rotation analysis, *Geophysics*, 75(3), F63–F70, doi:10.1190/1.3378765.
- Key, K., and J. Ovall (2011), A parallel goal-oriented adaptive finite element method for 2.5D electromagnetic modelling, *Geophys. J. Int.*, 186(1), 137–154, doi:10.1111/j.1365-246X.2011.05025.x.
- Kvenvolden, K. (1993), Gas Hydrates- geological perspective and global change, *Rev. Geophys.*, 31(2), 173–187.
- Kvenvolden, K. A. (1999), Potential effects of gas hydrate on human welfare, *Proc. Natl. Acad. Sci. U.S.A.*, 96(7), 3420–3426.
- Lewis, E. L., and R. G. Perkin (1981), The practical salinity scale 1978: Conversion of existing data, *Deep Sea Res.*, 28(4), 307–328.
- Li, Y., and S. Constable (2007), Special section - Marine control-source electromagnetic methods 2D marine controlled-source electromagnetic modeling: Part 2 - The effect of bathymetry, *Geophysics*, 72(2), WA63–WA71.
- Li, Y., and J. Pek (2008), Adaptive finite element modelling of two-dimensional magnetotelluric fields in general anisotropic media, *Geophys. J. Int.*, 175(3), 942–954, doi:10.1111/j.1365-246X.2008.03955.x.
- Liu, X., and P. B. Flemings (2006), Passing gas through the hydrate stability zone at southern Hydrate Ridge, offshore Oregon, *Earth Planet. Sci. Lett.*, 247(1–2), 211–226, doi:10.1016/j.epsl.2005.10.026.
- Liu, X., and P. B. Flemings (2007), Dynamic multiphase flow model of hydrate formation in marine sediments, *J. Geophys. Res.*, 112, B03101, doi:10.1029/2005JB004227.
- MacGregor, L., and J. Tomlinson (2014), Special section: Interpretation and integration of CSEM data Marine controlled-source electromagnetic methods in the hydrocarbon industry: A tutorial on method and practice, *Interpretation*, 2(3), 13–32.
- MacKay, M. E., R. D. Jarrard, G. K. Westbrook, and R. D. Hyndman (1994), Origin of bottom-simulating reflectors: Geophysical evidence from the Cascadia accretionary prism, *Geology*, 22, 459–462, doi:10.1130/0091-7613(1994)022<0459:OBSRG>2.3.CO;2.
- Mavko, G., T. Mukerji, and J. Dvorkin (2009), *The Rock Physics Handbook*, 1–511 pp., Cambridge Univ. Press, Cambridge, U. K.
- Minshull, T., M. Sinha, and C. Pierce (2005), Multi-disciplinary, sub-seabed geophysical imaging, *Sea Technol.*, 46(10), 27–31.
- Morten, J. P., A. K. Bjorke, and T. Storen (2009), CSEM data uncertainty analysis for 3D inversion SEG Houston 2009 International Exposition and Annual Meeting SEG Houston 2009 International Exposition and Annual Meeting, *SEG Houston International Exposition and Annual Meeting*, pp. 724–728, Houston, Tex.
- Murton, B., V. Huhnerbach, and J. Garrard (2012), Exploring ultradeep hydrothermal vents in the Cayman Trough by ROV, *Sea Technol.*, 53(9), 9–15.
- Myer, D., S. Constable, and K. Key (2011), Broad-band waveforms and robust processing for marine CSEM surveys, *Geophys. J. Int.*, 184, 689–698, doi:10.1111/j.1365-246X.2010.04887.x.
- Myer, D., S. Constable, K. Key, M. E. Glinsky, and G. Liu (2012), Marine CSEM of the Scarborough gas field, Part 1: Experimental design and data uncertainty, *Geophysics*, 77(4), E281–E299, doi:10.1190/geo2011-0380.1.
- Panieri, G., R. H. James, A. Camerlenghi, V. Cesari, C. S. Cervera, I. Cacho, and G. K. Westbrook (2014), Record of methane emissions from the West Svalbard continental margin during the last 16,000 years revealed by  $\delta^{13}\text{C}$  of benthic foraminifera, *Global Planet. Change*, 122, 151–160, doi:10.1016/j.gloplacha.2014.08.014.
- Paull, C. K., and R. Matsumoto (2000), Leg 164 Overview, in *Proceedings of the Ocean Drilling Program, Scientific Results*, vol. 164, edited by C. K. Paull et al., pp. 3–10, Ocean Drilling Program, College Station, Tex.
- Pearson, C. F., P. M. Halleck, P. L. McGuire, R. Hermes, and M. Mathews (1983), Natural gas hydrate deposits: A review of in situ properties, *J. Phys. Chem.*, 87(21), 4180–4185, doi:10.1021/j100244a041.
- Petersen, C. J., S. Bünz, S. Hustoft, J. Mienert, and D. Klaeschen (2010), High-resolution P-Cable 3D seismic imaging of gas chimney structures in gas hydrated sediments of an Arctic sediment drift, *Mar. Pet. Geol.*, 27(9), 1981–1994, doi:10.1016/j.marpetgeo.2010.06.006.
- Plaza-Faverola, A., G. K. Westbrook, S. Ker, R. J. K. Exley, A. Gailler, T. A. Minshull, and K. Broto (2010), Evidence from three-dimensional seismic tomography for a substantial accumulation of gas hydrate in a fluid-escape chimney in the Nyegga pockmark field, offshore Norway, *J. Geophys. Res.*, 115, B08104, doi:10.1029/2009JB007078.
- Ramananjaona, C., L. MacGregor, and D. Andréis (2011), Sensitivity and inversion of marine electromagnetic data in a vertically anisotropic stratified earth, *Geophys. Prospect.*, 59(2), 341–360, doi:10.1111/j.1365-2478.2010.00919.x.
- Revil, A., L. M. Cathles, S. Losh, and J. A. Nunn (1998), Electrical conductivity in shaly sands with geophysical applications, *J. Geophys. Res.*, 103(B10), 23,925–23,936, doi:10.1029/98JB02125.
- Ritzmann, O., W. Jokat, W. Czuba, A. Guterch, R. Mjelde, and Y. Nishimura (2004), A deep seismic transect from Hovgard Ridge to northwestern Svalbard across the continental-ocean transition: A sheared margin study, *Geophys. J. Int.*, 157, 683–702, doi:10.1111/j.1365-246X.2004.02204.x.

- Sarkar, S., C. Berndt, T. A. Minshull, G. K. Westbrook, D. Klaeschen, D. G. Masson, A. Chabert, and K. E. Thatcher (2012), Seismic evidence for shallow gas-escape features associated with a retreating gas hydrate zone offshore west Svalbard, *J. Geophys. Res.*, *117*, B09102, doi:10.1029/2011JB009126.
- Schwalenberg, K., E. Willoughby, R. Mir, and R. N. Edwards (2005), Marine gas hydrate electromagnetic signatures in Cascadia and their correlation with seismic blank zones, *First Break*, *23*, 57–63.
- Schwalenberg, K., M. Haeckel, J. Poort, and M. Jegen (2010), Evaluation of gas hydrate deposits in an active seep area using marine controlled source electromagnetics: Results from Opouawe Bank, Hikurangi Margin, New Zealand, *Mar. Geol.*, *272*(1–4), 79–88, doi:10.1016/j.margeo.2009.07.006.
- Sinha, M. C., P. D. Patel, M. J. Unsworth, T. R. E. Owen, M. R. G. Maccormack, and M. Road (1990), An active source electromagnetic sounding system for marine use, *Mar. Geophys. Res.*, *12*, 59–68.
- Sloan, E. D., and C. A. Koh (2008), *Clathrate Hydrates of Natural Gases* 3rd ed., CRC Press, Taylor & Francis Group, Boca Raton, London, New York, doi:10.1016/S0076-6895(09)70001-0.
- Sloan, E. D., S. Subramanian, P. N. Matthews, J. P. Lederhos, and A. A. Khokhar (1998), Quantifying hydrate formation and kinetic inhibition, *Ind. Eng. Chem. Res.*, *37*(9), 3124–3132.
- Smith, A. J., J. Mienert, S. Bünz, and J. Greinert (2014a), Thermogenic methane injection via bubble transport into the upper Arctic Ocean from the hydrate-charged Vestnesa Ridge, Svalbard, *Geochem. Geophys. Geosyst.*, *15*, 1945–1959, doi:10.1002/2013GC005179.
- Smith, A. J., P. B. Flemings, X. Liu, and K. Darnell (2014b), The evolution of methane vents that pierce the hydrate stability zone in the world's oceans, *J. Geophys. Res. Solid Earth*, *119*, 6337–6356, doi:10.1002/2013JB010686.
- Smith, B. D., and S. H. Ward (1974), On the computation of polarization ellipse parameters, *Geophysics*, *39*(6), 867–869.
- Sultan, N., et al. (2014), Pockmark formation and evolution in deep water Nigeria: Rapid hydrate growth versus slow hydrate dissolution, *J. Geophys. Res. Solid Earth*, *119*, 2679–2694, doi:10.1029/2010JB007453.
- Torres, M., K. Wallmann, A. Tréhu, G. Bohrmann, W. Borowski, and H. Tomaru (2004), Gas hydrate growth, methane transport, and chloride enrichment at the southern summit of Hydrate Ridge, Cascadia margin off Oregon, *Earth Planet. Sci. Lett.*, *226*(1–2), 225–241, doi:10.1016/j.epsl.2004.07.029.
- Tréhu, A., et al. (2004), Three-dimensional distribution of gas hydrate beneath southern Hydrate Ridge: Constraints from ODP Leg 204, *Earth Planet. Sci. Lett.*, *222*(3–4), 845–862, doi:10.1016/j.epsl.2004.03.035.
- Vanneste, M., S. Guidard, and J. Mienert (2005), Bottom-simulating reflections and geothermal gradients across the western Svalbard margin, *Terra Nova*, *17*(6), 510–516, doi:10.1111/j.1365-3121.2005.00643.x.
- Vogt, P. R., K. Crane, E. Sundvor, M. D. Max, and S. L. Pfirman (1994), Methane-generated (?) pockmarks on young, thickly sedimented oceanic crust in the Arctic: Vestnesa ridge, Fram strait, *Geology*, *22*, 255–258, doi:10.1130/0091-7613(1994)022<0255:MGPOYT>2.3.CO;2.
- Waxman, M. H., and L. J. M. Smits (1968), Electrical conductivities in oil-bearing shaly sands, *Soc. Pet. Eng. J.*, *8*, 107–122.
- Weitemeyer, K., and S. Constable (2010), Mapping shallow geology and gas hydrate with marine CSEM surveys, *First Break*, *28*, 97–102.
- Weitemeyer, K., G. Gao, S. Constable, and D. Alumbaugh (2010), The practical application of 2D inversion to marine controlled-source electromagnetic data, *Geophysics*, *75*(6), F199–F211.
- Weitemeyer, K. A., S. C. Constable, K. W. Key, and J. P. Behrens (2006b), First results from a marine controlled-source electromagnetic survey to detect gas hydrates offshore Oregon, *Geophys. Res. Lett.*, *33*, L03304, doi:10.1029/2005GL024896.
- Weitemeyer, K. A., S. Constable, and A. M. Tréhu (2011), A marine electromagnetic survey to detect gas hydrate at Hydrate Ridge, Oregon, *Geophys. J. Int.*, *187*(1), 45–62, doi:10.1111/j.1365-246X.2011.05105.x.
- Weitemeyer, K., and S. Constable (2014), Navigating marine electromagnetic transmitters using dipole field geometry, *Geophys. Prospect.*, *62*(3), 573–596, doi:10.1111/1365-2478.12092.
- Westbrook, G., et al. (2008), Estimation of gas hydrate concentration from multi-component seismic data at sites on the continental margins of NW Svalbard and the Storegga region of Norway, *Mar. Pet. Geol.*, *25*(8), 744–758, doi:10.1016/j.marpetgeo.2008.02.003.
- Westbrook, G. K., et al. (2009), Escape of methane gas from the seabed along the West Spitsbergen continental margin, *Geophys. Res. Lett.*, *36*, L15608, doi:10.1029/2009GL039191.
- Winsauer, W. O., H. M. Shearin, P. H. Masson, and M. Williams (1952), Resistivity of brine-saturated sands in relation to pore geometry, *AAPG Bull.*, *36*, 253–277.
- Wheelock, B. D. (2012), Electromagnetic imaging of the crust and upper mantle across the continental margin in central California, PhD thesis, Univ. of Calif., San Diego.
- Zelt, C., and R. Smith (1992), Seismic travel-time inversion for 2-D crustal structure, *Geophys. J. Int.*, *108*, 16–34, doi:10.1111/j.1365-246X.1992.tb00836.x.